A&A 611, A6 (2018)
https://doi.org/10.1051/0004-6361/201732168

Astronomy & Astrophysics

ATLASGAL-selected massive clumps in the inner Galaxy*

VI. Kinetic temperature and spatial density measured with formaldehyde

X. D. Tang[1,2,3], C. Henkel[1,4], F. Wyrowski[1], A. Giannetti[1,5], K. M. Menten[1], T. Csengeri[1], S. Leurini[1,6], J. S. Urquhart[1,7], C. König[1], R. Güsten[1], Y. X. Lin[1], X. W. Zheng[8], J. Esimbek[2,3], and J. J. Zhou[2,3]

[1] Max-Planck-Institut für Radioastronomie, Auf dem Hügel 69, 53121 Bonn, Germany
e-mail: xdtang@mpifr-bonn.mpg.de
[2] Xinjiang Astronomical Observatory, Chinese Academy of Sciences, 830011 Urumqi, PR China
[3] Key Laboratory of Radio Astronomy, Chinese Academy of Sciences, 830011 Urumqi, PR China
[4] Astronomy Department, King Abdulaziz University, PO Box 80203, 21589 Jeddah, Saudi Arabia
[5] INAF–Istituto di Radioastronomia & Italian ALMA Regional Centre, Via P. Gobetti 101, 40129 Bologna, Italy
[6] INAF–Osservatorio Astronomico di Cagliari, Via della Scienza 5, 09047 Selargius (CA), Italy
[7] School of Physical Sciences, University of Kent, Ingram Building, Canterbury, Kent CT2 7NH, UK
[8] School of Astronomy and Space Science, Nanjing University, 210093 Nanjing, PR China

Received 25 October 2017 / Accepted 27 November 2017

ABSTRACT

Context. Formaldehyde (H_2CO) is a reliable tracer to accurately measure the physical parameters of dense gas in star-forming regions.
Aims. We aim to determine directly the kinetic temperature and spatial density with formaldehyde for the ~100 brightest ATLASGAL-selected clumps (the TOP100 sample) at 870 μm representing various evolutionary stages of high-mass star formation.
Methods. Ten transitions (J = 3–2 and 4–3) of ortho- and para-H_2CO near 211, 218, 225, and 291 GHz were observed with the Atacama Pathfinder EXperiment (APEX) 12 m telescope.
Results. Using non-LTE models with RADEX, we derived the gas kinetic temperature and spatial density with the measured para-H_2CO 3_{21}–2_{20}/3_{03}–2_{02}, 4_{22}–3_{21}/4_{04}–3_{03}, and 4_{04}–3_{03}/3_{03}–2_{02} ratios. The gas kinetic temperatures derived from the para-H_2CO 3_{21}–2_{20}/3_{03}–2_{02} and 4_{22}–3_{21}/4_{04}–3_{03} line ratios are high, ranging from 43 to >300 K with an unweighted average of 91 ± 4 K. Deduced $T_{\rm kin}$ values from the J = 3–2 and 4–3 transitions are similar. Spatial densities of the gas derived from the para-H_2CO 4_{04}–3_{03}/3_{03}–2_{02} line ratios yield 0.6–8.3 × 10^6 cm^{-3} with an unweighted average of 1.5 (±0.1) × 10^6 cm^{-3}. A comparison of kinetic temperatures derived from para-H_2CO, NH_3, and dust emission indicates that para-H_2CO traces a distinctly higher temperature than the NH_3 (2, 2)/(1, 1) transitions and the dust, tracing heated gas more directly associated with the star formation process. The H_2CO line widths are found to be correlated with bolometric luminosity and increase with the evolutionary stage of the clumps, which suggests that higher luminosities tend to be associated with a more turbulent molecular medium. It seems that the spatial densities measured with H_2CO do not vary significantly with the evolutionary stage of the clumps. However, averaged gas kinetic temperatures derived from H_2CO increase with time through the evolution of the clumps. The high temperature of the gas traced by H_2CO may be mainly caused by radiation from embedded young massive stars and the interaction of outflows with the ambient medium. For $L_{\rm bol}/M_{\rm clump} \gtrsim 10\, L_\odot/M_\odot$, we find a rough correlation between gas kinetic temperature and this ratio, which is indicative of the evolutionary stage of the individual clumps. The strong relationship between H_2CO line luminosities and clump masses is apparently linear during the late evolutionary stages of the clumps, indicating that $L_{\rm H_2CO}$ does reliably trace the mass of warm dense molecular gas. In our massive clumps H_2CO line luminosities are approximately linearly correlated with bolometric luminosities over about four orders of magnitude in $L_{\rm bol}$, which suggests that the mass of dense molecular gas traced by the H_2CO line luminosity is well correlated with star formation.

Key words. stars: formation – stars: massive – ISM: clouds – ISM: molecules – ISM: abundances – radio lines: ISM

1. Introduction

In the Galactic disk, star formation appears to occur only in dense regions (spatial density $n(H_2) \gtrsim 10^4$ cm^{-3}) composed of molecular gas (Lada et al. 2010; Ginsburg et al. 2015). High-mass stars form in massive clumps with typical size of order ~1 pc (e.g. Dunham et al. 2010, 2011; Rosolowsky et al. 2010; Urquhart et al. 2014; He et al. 2015; Wienen et al. 2015; König et al. 2017; Yuan et al. 2017). High-mass stars influence the surrounding environment and subsequent star formation through their feedback such as outflows, winds, and UV radiation. However, the details of high-mass star formation process and how their feedback may affect the initial conditions of high-mass stars in their formation process are still far from clear and require, as a basis, the precise determination of kinetic temperature and density.

The Atacama Pathfinder EXperiment (APEX) Telescope Large Area Survey of the GALaxy (ATLASGAL; Schuller et al. 2009), presenting observations in a Galactic longitude and latitude range of ±60° and ±1.5°, respectively, introduces a global view on star formation at 870 μm and identifies ~10 000 massive clumps in various stages of evolution undergoing high-mass star formation in the inner Galaxy (Contreras et al. 2013; Urquhart et al. 2014, 2018; Csengeri et al. 2014). The most

* Source and H_2CO parameters (Tables A.1–A.7) are only available at the CDS via anonymous ftp to cdsarc.u-strasbg.fr (130.79.128.5) or via http://cdsarc.u-strasbg.fr/viz-bin/qcat?J/A+A/611/A6

fundamental physical parameters, kinetic temperature and spatial density of the clumps, affect chemistry, star formation, and could also impact the stellar initial mass function. Accurate measurements of these physical parameters are indispensable for a general understanding of the physical processes involved in these massive star-forming clumps.

Formaldehyde (H_2CO) is a ubiquitous molecule in interstellar clouds (Downes et al. 1980; Bieging et al. 1982; Henkel et al. 1991; Zylka et al. 1992; Mangum et al. 2008, 2013a; Ao et al. 2013; Tang et al. 2013; Ginsburg et al. 2015, 2016, 2017; Guo et al. 2016). As a slightly asymmetric rotor molecule, H_2CO exhibits a large number of millimetre and submillimetre transitions. This molecule is a reliable tracer of physical conditions such as temperature and density (Henkel et al. 1980, 1983; Mangum & Wootten 1993; Mühle et al. 2007; Ginsburg et al. 2011, 2015, 2016; Ao et al. 2013). Since the relative populations of the K_a ladders of H_2CO are predominantly governed by collisions, ratios of H_2CO line fluxes involving different K_a ladders are good tracers of the kinetic temperature, such as para-H_2CO $J_{K_aK_c} = 3_{22}$–$2_{21}/3_{03}$–2_{02}, 4_{23}–$3_{22}/4_{04}$–3_{03}, and 5_{23}–$4_{22}/5_{05}$–4_{04} (Mangum & Wootten 1993). Once the kinetic temperature is known, line ratios involving the same K_a ladders yield estimates of the spatial density of the gas, such as $J_{K_aK_c} = 4_{04}$–$3_{03}/3_{03}$–2_{02}, 5_{05}–$4_{04}/3_{03}$–2_{02}, and 5_{24}–$4_{23}/3_{22}$–2_{21} (Mangum & Wootten 1993; Mühle et al. 2007; Immer et al. 2016). Transitions connecting the same rotational levels (e.g. $J = 3$–2 or 4–3) and belonging to either the para- or ortho-H_2CO subspecies, but being part of different K_a ladders (e.g. $K_a = 0$, 2) are particularly useful. These transitions can be measured simultaneously with the same receiver system and their relative strengths (para-H_2CO 3_{22}–$2_{21}/3_{03}$–2_{02}, 3_{21}–$2_{20}/3_{03}$–2_{02}, 4_{23}–$3_{22}/4_{04}$–3_{03}, and 4_{22}–$3_{21}/4_{04}$–3_{03}) provide sensitive thermometry. Para-H_2CO is therefore possibly the best of the very few molecular tracers that are available for such an analysis of the dense molecular gas. H_2CO line ratios have been used to measure physical parameters in our Galactic centre clouds (Qin et al. 2008; Ao et al. 2013; Johnston et al. 2014; Ginsburg et al. 2016; Immer et al. 2016; Lu et al. 2017), star formation regions (Mangum & Wootten 1993; Hurt et al. 1996; Mangum et al. 1999; Mitchell et al. 2001; Watanabe & Mitchell 2008; Nagy et al. 2012; Lindberg et al. 2015; Tang et al. 2017a, 2018), and in external galaxies (Mühle et al. 2007; Tang et al. 2017b).

In this work, we aim to directly measure the kinetic temperature and spatial density towards massive star-forming clumps selected from the ATLASGAL survey making use of the rotational transitions of H_2CO ($J = 3$–2 and 4–3). Our main goals are (a) comparing kinetic temperatures from the gas to temperature estimates based on the dust; (b) searching for a correlation between kinetic temperature and line width, which is expected in the case of conversion of turbulent energy into heat; (c) seeking links between kinetic temperature and star formation rate (SFR) and the evolutionary stage of the massive star-forming regions; and (d) testing the star formation law by correlating the luminosity of the H_2CO lines to infrared luminosity.

In Sects. 2 and 3, we describe the measured samples, our H_2CO observations, and the data reduction, and introduce the main results. The discussion is presented in Sect. 4. Our main conclusions are summarized in Sect. 5.

2. Sample, observations, and data reduction

We selected the 110 brightest clumps from the ATLASGAL survey (the TOP100 sample) obeying simple IR criteria to cover a range in evolutionary stages as described in Giannetti et al. (2014) and König et al. (2017). These clumps consist almost entirely of clumps that have the potential to form, or are forming, massive stars. Depending on their IR and radio continuum properties, the sample of potentially high-mass star-forming clumps at various evolutionary stages can be separated into four categories: 70 μm weak sources (70w), infrared weak clumps (IRw), infrared bright objects (IRb), and sources containing compact H II regions (H II) (Giannetti et al. 2014; König et al. 2017). Previous work on this sample addressed SiO emission (for parts of the sample, Csengeri et al. 2016), dust continuum characterization (König et al. 2017), millimetre hydrogen recombination lines (for more evolved (i.e. H II regions) parts of the sample; Kim et al. 2017), and temperature structure (Giannetti et al. 2017). The TOP100 is an ideal sample to study the physical and chemical parameters of the potentially massive star-forming regions at various evolutionary stages.

Sources observed are listed in Table A.1. Our observations were carried out on 2013 July and December, 2014 September and November, and 2015 April, June, July, and October with the APEX[1] 12 m telescope located on Chajnantor (Chile). Specific observational details of the 10 measured transitions of H_2CO are listed in Table 1. Five transitions of H_2CO ($J = 3$–2) were observed with the new MPIfR 1-mm receiver (PI230) with a beam size from 27.6″ to 29.5″ and integration times of

Table 1. Observed H_2CO transition parameters.

Transition	Frequency GHz	E_u K	Receiver	Beam size arcsec
o-H_2CO 3_{13}–2_{12}	211.212	32.06	PI230	29.5
p-H_2CO 3_{03}–2_{02}	218.222	20.96	PI230	28.6
p-H_2CO 3_{22}–2_{21}	218.476	68.09	PI230	28.6
p-H_2CO 3_{21}–2_{20}	218.760	68.11	PI230	28.5
o-H_2CO 3_{12}–2_{11}	225.699	33.45	PI230	27.6
p-H_2CO 4_{04}–3_{03}	290.623	34.90	FLASH	21.5
p-H_2CO 4_{23}–3_{22}	291.238	82.07	FLASH	21.4
o-H_2CO 4_{32}–3_{31}	291.381	140.94	FLASH	21.4
o-H_2CO 4_{31}–3_{30}	291.384	140.94	FLASH	21.4
p-H_2CO 4_{22}–3_{21}	291.948	82.12	FLASH	21.4

Table 2. Observed H_2CO transitions and detection rates.

Transition	Observed	Detection	Detection rate
o-H_2CO 3_{13}–2_{12}	94	91	97%
p-H_2CO 3_{03}–2_{02}	94	92	98%
p-H_2CO 3_{22}–2_{21}	94	65	69%
p-H_2CO 3_{21}–2_{20}	94	66	70%
o-H_2CO 3_{12}–2_{11}	94	93	99%
p-H_2CO 4_{04}–3_{03}	98	97	99%
p-H_2CO 4_{23}–3_{22}	98	80	82%
o-H_2CO 4_{32}–3_{31}	98	83	85%
o-H_2CO 4_{31}–3_{30}	98	83	85%
p-H_2CO 4_{22}–3_{21}	98	83	85%

[1] This publication is based on data acquired with the Atacama Pathfinder EXperiment (APEX). APEX is a collaboration between the Max-Planck-Institut für Radioastronomie, the European Southern Observatory, and the Onsala Space Observatory.

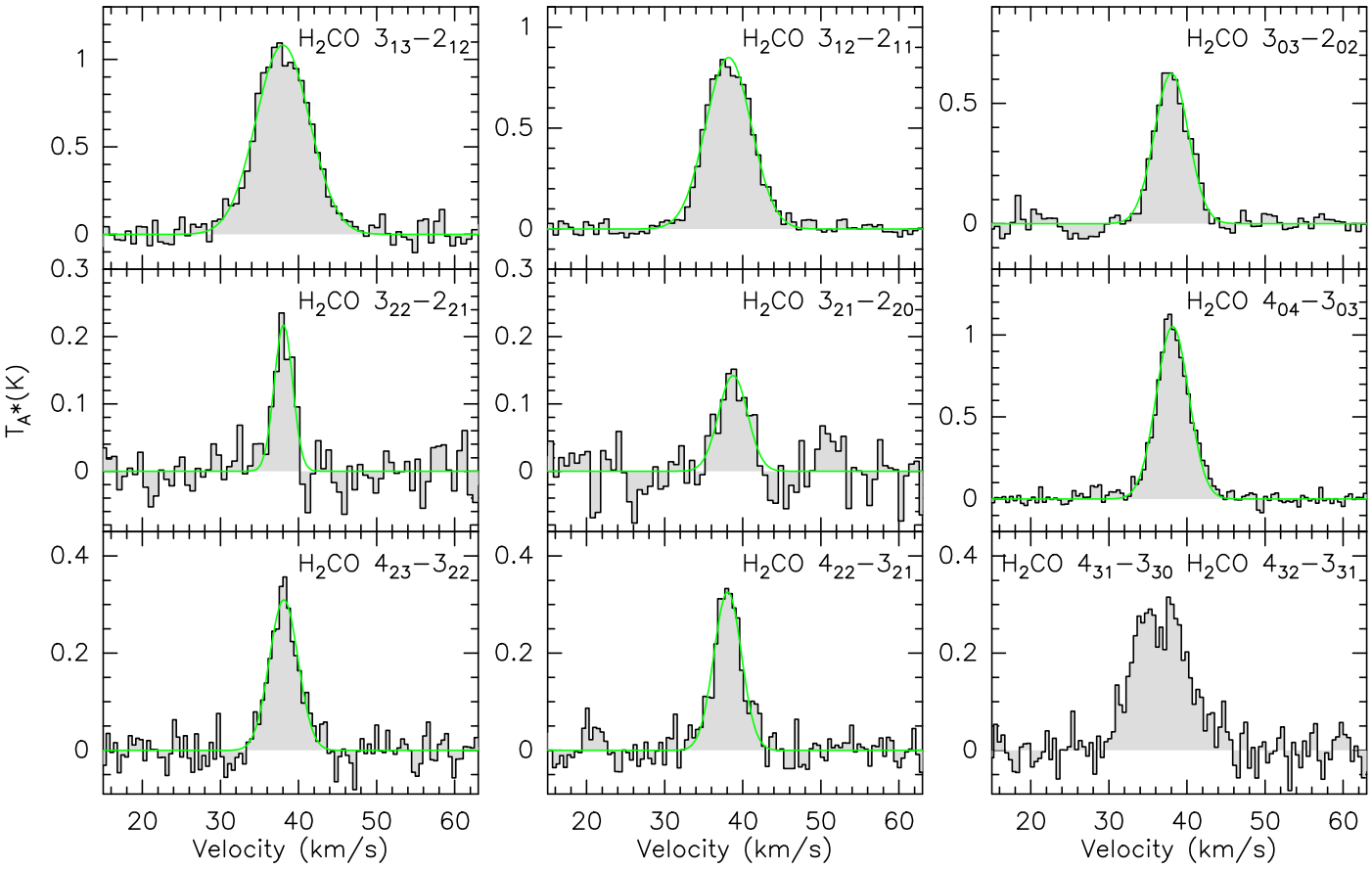

Fig. 1. Observed H_2CO spectra (grey) towards AGAL008.684−00.367. Green lines indicate the Gaussian fit results.

1–3 min. Five H_2CO ($J = 4$–3) transitions were observed with the FLASH receiver with a beam size ∼21.4″ and integration times of 2–4 min. For the PI230 receiver, we used a fast fourier transform spectrometer (FFTS4G) backend with two sidebands (lower and upper). Each sideband has two spectral windows of 4 GHz bandwidth, providing both orthogonal polarizations and leading to a total bandwidth of 8 GHz. An eXtended bandwidth fast fourier transform spectrometer (XFFTS) backend with two spectral windows of 2.5 GHz bandwidth leading to a total bandwidth of 4 GHz was used for the FLASH receiver. These provided velocity resolutions of ∼0.08 km s^{-1} for H_2CO ($J = 3$–2) and ∼0.04 km s^{-1} for H_2CO ($J = 4$–3). The observations were performed in position-switching mode with off positions offset from the on position of the sources by (600″, ±600″). We converted the antenna temperatures of the spectra into main beam brightness temperatures for both H_2CO $J = 3$–2 and 4–3 lines using a factor of 1/0.69. Observed continuum of Mars, Jupiter, and Saturn were used to calibrate the spectral line flux. The calibration uncertainty is about 20%.

Data reduction of spectral lines was performed using CLASS from the GILDAS package[2]. To enhance signal-to-noise ratios (S/N) in individual channels, we smoothed contiguous channels to a velocity resolution of ∼0.6 km s^{-1}. The line widths tend to be > few km s^{-1}, so the smoothing has no impact on our results. The typical noise level is ∼0.06 K (T_{mb} scale) for both H_2CO ($J = 3$–2) and H_2CO ($J = 4$–3) at a velocity resolution of ∼0.6 km s^{-1}.

[2] http://www.iram.fr/IRAMFR/GILDAS

3. Results

3.1. Overview

Ninety-four sources with H_2CO ($J = 3$–2) transitions and 98 sources with H_2CO ($J = 4$–3) transitions were observed. Nearly all H_2CO lines are detected (detection rate $\gtrsim$ 97%) for the upper energy above ground state, E_u, (<35 K) towards the targeted massive clumps (see Table 2). For high E_u (>82 K), the H_2CO detection rate ranges from 82% to 85%. Non-detections are associated with 70w and IRw sources (see Sect. 2 for the definitions), which are typically associated with the early cold evolutionary stages of massive clumps. Two para-H_2CO (3_{22}–2_{21} and 3_{21}–2_{20}) transitions ($E_u \sim 68$ K) show a lower detection rate (∼70%), which is caused by the fact that para-H_2CO is the less abundant of the two H_2CO symmetry species and the source of the weaker $K = 2$ transitions. High detection rates of H_2CO indicate that this species is commonly formed in massive star-forming clumps and is present during all their evolutionary stages.

Examples of H_2CO line spectra are presented in Fig. 1. Line parameters are listed in Tables A.2–A.5, where velocity-integrated intensity, $\int T_{mb} dv$, local standard of rest velocity, V_{lsr}, full width to half maximum line width (FWHM), and peak main beam brightness temperature, T_{mb}, were obtained from Gaussian fits. The rest frequencies of the ortho-H_2CO 4_{32}–3_{31} and 4_{31}–3_{30} transitions are nearby (see Table 1 and Fig. 1). These two lines are blended in all of our sources, so that Gaussian fits are of limited value and are not part of our tables.

3.2. Source size correction

The para-H_2CO $J = 3$–2 (beam size $\sim 28.6''$) and 4–3 (beam size $\sim 21.5''$) lines we observed were obtained by single pointing observations with different receivers, so the area covered by our $J = 3$–2 and 4–3 transitions is slightly different. We compare the integrated intensities of H_2CO, irrespective of the beam size with 870 μm flux densities in Fig. 2. This comparison shows that the H_2CO integrated intensities follow the 870 μm intensity distribution. Apparently dense gas traced by H_2CO is associated well with the dust traced by 870 μm emission in the massive star-forming clumps. Mapping observations of para-H_2CO (3_{03}–2_{02}, 3_{22}–2_{21}, and 3_{21}–2_{20}) towards the Orion molecular cloud 1 (OMC1) with the APEX telescope also show that para-H_2CO integrated intensity distributions agree well with the dust emission observed at 850 μm (Johnstone & Bally 1999; Tang et al. 2018). Previous observations of H_2CO (4_{04}–3_{03}, 4_{23}–3_{22}, 4_{22}–3_{21}, 4_{32}–3_{31}, and 4_{31}–3_{30}) towards massive clumps in the W33 region with the APEX telescope (Immer et al. 2014) also indicate that H_2CO distributions are consistent with the dust emission traced by 870 μm. Hence, we assume that the source sizes of H_2CO are the same as the full width to half power source sizes of the 870 μm dust emission derived from Csengeri et al. (2014). We correct for beam dilution by calculating $T'_{\rm mb} = T_{\rm mb}/\eta_{\rm bf}$ with beam-filling factor $\eta_{\rm bf} = \theta_{\rm s}^2/(\theta_{\rm s}^2+\theta_{\rm beam}^2)$. Here $\theta_{\rm beam}$ and $\theta_{\rm s}$ denote beam and source size, respectively. The results of $\eta_{\rm bf}$ and the para-H_2CO 4_{04}–3_{03}/3_{03}–2_{02} integrated intensity ratio ($I'(4_{04}$–$3_{03})/I'(3_{03}$–$2_{02})$) corrected with $\eta_{\rm bf}$ are listed in Table A.6.

3.3. Opacities of H_2CO

To determine the gas kinetic temperatures, $T_{\rm kin}$, spatial densities, $n(H_2)$, and para-H_2CO column densities, $N(H_2CO)$, we used the RADEX non-LTE model (van der Tak et al. 2007) offline code[3] with collision rates from Wiesenfeld & Faure (2013). Uncertainties in the collisional excitation rates directly affect the derived volume densities, while kinetic temperature appears to be less affected by collisional excitation rate uncertainties (see Sect. 3.4). The RADEX code needs five input parameters: background temperature, kinetic temperature, H_2 density, H_2CO column density, and line width. For the background temperature, we adopted 2.73 K. Model grids for the H_2CO lines encompass 40 densities ($n(H_2) = 10^4$–10^8 cm^{-3}), 40 H_2CO column densities ($N(H_2CO) = 10^{12}$–10^{16} cm^{-2}), and 40 temperatures ranging from 10 to 400 K. For the line width, we used the observed line width value.

The value of N(para-H_2CO) depends on para-H_2CO 3_{03}–2_{02} and/or 4_{04}–3_{03} integrated intensities and the para-H_2CO 4_{04}–3_{03}/3_{03}–2_{02} ratio (Mangum & Wootten 1993; Tang et al. 2017a). If the para-H_2CO 3_{03}–2_{02} and 4_{04}–3_{03} lines are optically thick in our dense massive clumps, this would cause high para-H_2CO 4_{04}–3_{03}/3_{03}–2_{02}, 3_{21}–2_{20}/3_{03}–2_{02}, and 4_{22}–3_{21}/4_{04}–3_{03} ratios. Higher ratios imply higher spatial densities and kinetic temperatures, respectively (Mangum & Wootten 1993; Ao et al. 2013; Ginsburg et al. 2016; Immer et al. 2016; Tang et al. 2017a,b, 2018). In order to understand the impact of the line optical depth, we modelled the optical depth of para-H_2CO 3_{03}–2_{02} and para-H_2CO 4_{04}–3_{03} integrated intensities, and the para-H_2CO 4_{04}–3_{03}/3_{03}–2_{02} ratio at a kinetic temperature of 55 K (see Sect. 3.4) in Fig. 3 (or see Fig. G.2 in Immer et al. 2016). Changing the kinetic temperature, weakly affects the optical depth of the para-H_2CO 3_{03}–2_{02} and para-H_2CO 4_{04}–3_{03} lines (less than by a factor of few). The para-H_2CO 4_{04}–3_{03}/3_{03}–2_{02} ratio is then also not greatly changed ($\lesssim$30%; not shown here). The figure demonstrates that para-H_2CO 3_{03}–2_{02} is optically thin ($\tau < 1$) at column density N(para-H_2CO) $< 1\times10^{14}$ cm^{-2} and spatial density 10^{4-8} cm^{-3}. At higher column density (N(para-H_2CO) $> 5\times10^{14}$ cm^{-2}), the para-H_2CO 3_{03}–2_{02} becomes optically thick ($\tau > 5$). The optical depth of para-H_2CO 4_{04}–3_{03} shows a similar behaviour (slightly lower values) with respect to that of para-H_2CO 3_{03}–2_{02} (not shown here; or see Fig. G.2 in Immer et al. 2016). Considering the observed ranges of integrated intensities of para-H_2CO 4_{04}–3_{03} (typical value $\sim$20 K km s^{-1}) and para-H_2CO 4_{04}–3_{03}/3_{03}–2_{02} ratios (typical value $\sim$1.0) accounting for relevant beam-filling factors from Sect. 3.2 (see Tables A.4 and A.6), the optical depths of para-H_2CO 3_{03}–2_{02} and 4_{04}–3_{03} range from $\sim$0.012 to $\sim$1 in our sample. Compared to the para-H_2CO 3_{03}–2_{02} and 4_{04}–3_{03} lines, para-H_2CO 3_{22}–2_{21}, 3_{21}–2_{20}, 4_{23}–3_{22}, and 4_{22}–3_{21} lines have higher upper energies above the ground state ($E_{\rm u} > 68$ K, see Table 1), so they have lower optical depths ($\tau \ll 1$). Therefore, the influence of the para-H_2CO 3_{03}–2_{02} and 4_{04}–3_{03} optical depths is weak for our determination of spatial density and kinetic temperature.

In our sample the observed $T_{\rm mb}(3_{12}$–$2_{11}/3_{03}$–$2_{02})$ ratios range from 0.74 to 1.83 with an unweighted average of 1.29 ± 0.02 (see Tables A.2 and A.3; errors given here and elsewhere are standard deviations of the mean). For the $T_{\rm mb}(3_{13}$–$2_{12}/3_{03}$–$2_{02})$ ratio, it ranges from 1.03 to 2.35 with an unweighted average of 1.56 ± 0.03 (see Tables A.2 and A.3). The relation between $T_{\rm mb}(3_{12}$–$2_{11}/3_{03}$–$2_{02})$ and H_2CO optical depth, indicated by Sasselov & Rucinski (1990) in their Fig. 2, suggests that for at least 30% of our sample ($T_{\rm mb}(3_{12}$–$2_{11}/3_{03}$–$2_{02}) \lesssim 1.19$) the ortho-H_2CO 3_{12}–2_{11} and 3_{13}–2_{12} lines are optically thick ($\tau \gtrsim 5$).

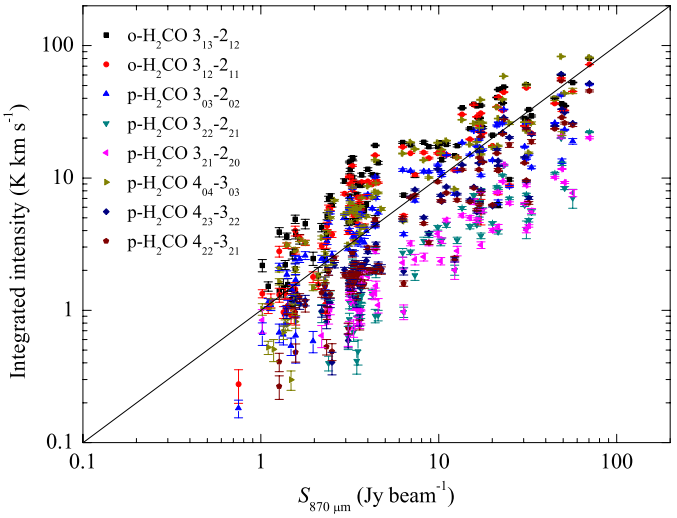

Fig. 2. Comparison of integrated intensities of H_2CO and 870 μm continuum flux densities. The solid line corresponds to $Y = X$ in the given units.

3.4. Kinetic temperature

As discussed in Sect. 1, the intensity ratios of H_2CO lines involving different $K_{\rm a}$ ladders yield estimates of the kinetic temperature of the gas (Mangum & Wootten 1993). For our observed transitions of H_2CO, para-H_2CO 3_{21}–2_{20}/3_{03}–2_{02}, 3_{22}–2_{21}/3_{03}–2_{02}, 4_{22}–3_{21}/4_{04}–3_{03}, and 4_{23}–3_{22}/4_{04}–3_{03} ratios can be useful

[3] http://var.sron.nl/radex/radex.php

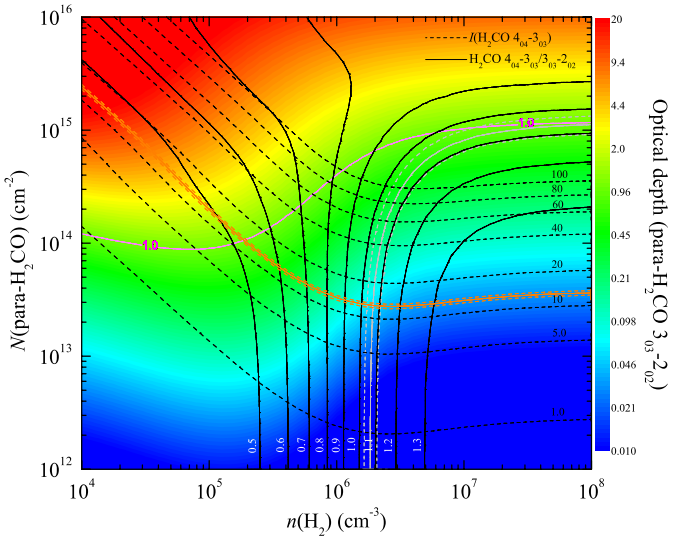

Fig. 3. Example of RADEX non-LTE modelling of the $N(H_2CO)$–$n(H_2)$ relation for AGAL008.684−00.367 at a kinetic temperature of 55 K (see Sect. 3.4). Black dashed and solid lines are para-H_2CO 4_{04}–3_{03} integrated intensities and para-H_2CO 4_{04}–$3_{03}/3_{03}$–2_{02} integrated intensity ratios, respectively. To the measured parameters, para-H_2CO 4_{04}–3_{03} integrated intensity (orange solid and dashed lines represent observed value and uncertainty) and para-H_2CO 4_{04}–$3_{03}/3_{03}$–2_{02} integrated intensity ratio (white solid and dashed lines) are corrected by the relevant beam-filling factors (see Table A.6). The colour map shows the optical depth of the para-H_2CO 3_{03}–2_{02} line. The purple line in the upper green area corresponds to optical depth τ(para-H_2CO 3_{03}–2_{02}) = 1.0.

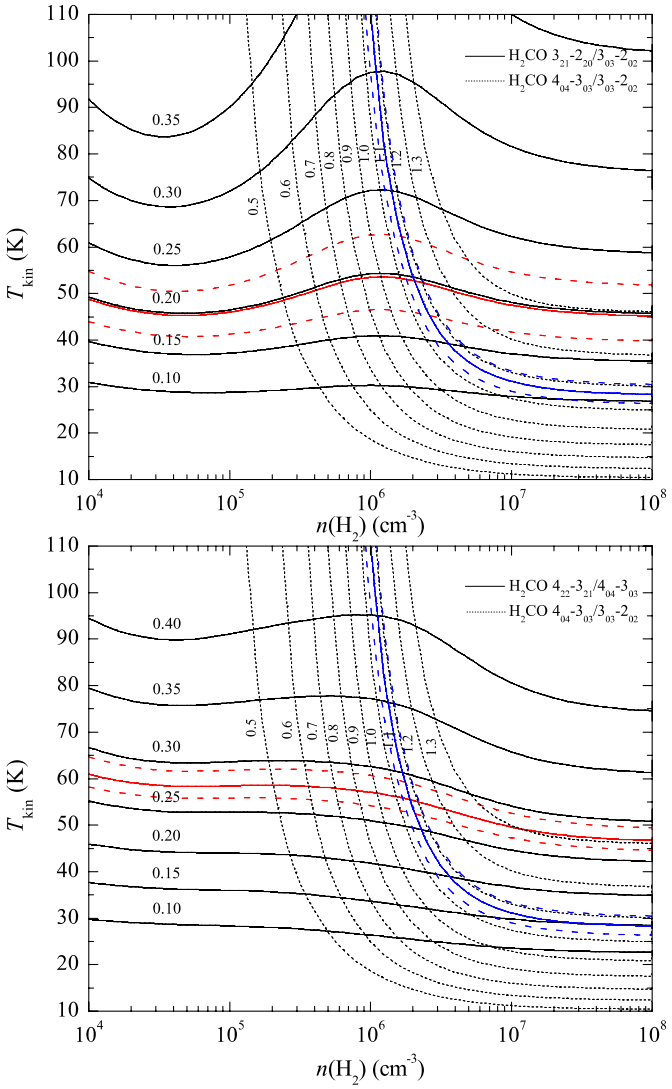

Fig. 4. Example of RADEX non-LTE modelling of the para-H_2CO kinetic temperature for AGAL008.684−00.367. Black solid and dashed lines are para-H_2CO integrated intensity ratios. Para-H_2CO 4_{04}–$3_{03}/3_{03}$–2_{02} (blue solid and dashed lines represent observed value and uncertainty, accounting for different beam-filling factors), 3_{21}–$2_{20}/3_{03}$–2_{02} and 4_{22}–$3_{21}/4_{04}$–3_{03} integrated intensity ratios (*top and bottom*, red solid and dashed lines) for a para-H_2CO column density 2.8×10^{13} cm^{-2} are derived from the para-H_2CO 4_{04}–3_{03} integrated intensity and para-H_2CO 4_{04}–$3_{03}/3_{03}$–2_{02} ratio (see Sect. 3.3).

thermometers to derive the kinetic temperature. Para-H_2CO 3_{22}–$2_{21}/3_{03}$–2_{02} and 3_{21}–$2_{20}/3_{03}$–2_{02} ratios trace the kinetic temperature with an uncertainty of $\lesssim$25% below 50 K (Mangum & Wootten 1993). Para-H_2CO 4_{22}–$3_{21}/4_{04}$–3_{03} and 4_{23}–$3_{22}/4_{04}$–3_{03} ratios trace the kinetic temperature with an uncertainty of $\lesssim$25% below 75 K (Mangum & Wootten 1993). The para-H_2CO 3_{22}–$2_{21}/3_{03}$–2_{02} and 4_{23}–$3_{22}/4_{04}$–3_{03} line ratios are slightly affected by the spatial density (not shown here; for para-H_2CO 3_{22}–$2_{21}/3_{03}$–2_{02} see Lindberg et al. 2015 and Tang et al. 2017a). Therefore in this work we use the para-H_2CO 3_{21}–$2_{20}/3_{03}$–2_{02} and 4_{22}–$3_{21}/4_{04}$–3_{03} integrated intensity ratios to derive the kinetic temperature, which also have been used for the Galactic central molecular zone (CMZ) clouds (Ginsburg et al. 2016; Immer et al. 2016).

We ran RADEX to calculate the observed para-H_2CO 3_{21}–$2_{20}/3_{03}$–2_{02}, 4_{22}–$3_{21}/4_{04}$–3_{03}, and 4_{04}–$3_{03}/3_{03}$–2_{02} integrated intensity ratios corrected by the relevant beam-filling factors assuming these transitions of para-H_2CO are optically thin (see Sect. 3.3). In Fig. 4, an example is presented to show how the parameters are constrained by the line ratio distribution of para-H_2CO, accounting for different beam-filling factors in the T_{kin}–$n(H_2)$ parameter space. We used the column density derived from the para-H_2CO 4_{04}–3_{03} integrated intensity and para-H_2CO 4_{04}–$3_{03}/3_{03}$–2_{02} ratio accounting for the beam-filling factors derived in Sect. 3.2 to constrain the kinetic temperature. Figure 4 shows that para-H_2CO 3_{21}–$2_{20}/3_{03}$–2_{02} and 4_{22}–$3_{21}/4_{04}$–3_{03} line ratios are sensitive to the gas kinetic temperature (see the black solid lines in Fig. 4), while being relatively independent of spatial density. The integrated intensity ratio $I'(4_{04}$–$3_{03})/I'(3_{03}$–$2_{02})$ is sensitive to the gas spatial density at high temperature ($T_{kin} > 40$ K), where the $I'(4_{04}$–$3_{03})/I'(3_{03}$–$2_{02})$ ratio becomes relatively independent of kinetic temperature. At low temperature ($T_{kin} < 40$ K), this ratio is influenced almost entirely by the gas kinetic temperature because T_{kin} becomes lower than the excitation difference of the involved states. Therefore, para-H_2CO 3_{21}–$2_{20}/3_{03}$–2_{02} and 4_{22}–$3_{21}/4_{04}$–3_{03} ratios combined with the para-H_2CO 4_{04}–$3_{03}/3_{03}$–2_{02} ratio are good tracers to constrain kinetic temperature and spatial density of dense gas in warm regions (gas temperature >30 K, for lower T_{kin} the levels of the $J = 3$–2 and 4–3 $K_a > 0$ lines are too far above the ground state) of massive star-forming clumps. Because the two $J = 4$, $K_a = 2$ levels are located 80–90 K above the ground state (see Table 1), the radiative transfer models start to become insensitive to temperatures in excess of 150 K. Hence, temperatures >150 K have to be considered sceptically and should cautiously be interpreted as $\gtrsim$150 K (Mangum & Wootten 1993; Ginsburg et al. 2016; Immer et al. 2016). The derived kinetic temperatures are listed in Table A.6.

We note a para-H_2CO 3_{21}–2_{20}/3_{03}–2_{02} ratio bump at kinetic temperature >50 K and spatial density $10^{5.5-7.0}$ cm^{-3} in Fig. 4 (or see Fig. 13 in Mangum & Wootten (1993) and Fig. F.1 in Lindberg et al. (2015)) because the excitation temperature of the para-H_2CO 3_{21}–2_{20} line rises much faster than that of the para-H_2CO 3_{03}–2_{02} line with increasing spatial density and/or kinetic temperature (Mangum & Wootten 1993). Kinetic temperatures obtained for a given para-H_2CO 3_{21}–2_{20}/3_{03}–2_{02} ratio vary more than by $\gtrsim$20% at kinetic temperature >60 K and spatial density $10^{5.0-7.0}$ cm^{-3}. This large "bump" in the para-H_2CO 3_{21}–2_{20}/3_{03}–2_{02} contour (see Fig. 4 upper panel) probably leads to an overestimate of the kinetic temperature from the para-H_2CO 3_{21}–2_{20}/3_{03}–2_{02} ratio. Para-H_2CO 4_{22}–3_{21}/4_{04}–3_{03} is also influenced by a bump, this time at kinetic temperature >100 K and spatial density $10^{5.5-7.0}$ cm^{-3} (see Fig. 4 lower panel or Fig. 13 in Mangum & Wootten 1993). Kinetic temperatures derived from the para-H_2CO 4_{22}–3_{21}/4_{04}–3_{03} ratio vary less than $\lesssim$20% for $T_{\rm kin}$ < 150 K and spatial density $10^{5.0-7.0}$ cm^{-3}. It appears that the para-H_2CO 4_{22}–3_{21}/4_{04}–3_{03} ratio is more stable and accurate to trace gas kinetic temperature than the para-H_2CO 3_{21}–2_{20}/3_{03}–2_{02} ratio at $T_{\rm kin}$ < 150 K and spatial density $10^{5.0-7.0}$ cm^{-3}.

A comparison of kinetic temperatures derived from both para-H_2CO 3_{21}–2_{20}/3_{03}–2_{02} and 4_{22}–3_{21}/4_{04}–3_{03} ratios suggests that the two ratios trace similar temperatures (see Fig. 5). It might have been expected, for example by analogy to NH_3 (e.g. Henkel et al. 1987; Mangum et al. 2013a; Gong et al. 2015a,b), that higher excited H_2CO transitions lead to higher $T_{\rm kin}$ values. Some of the similar kinetic temperatures derived from the para-H_2CO 3_{21}–2_{20}/3_{03}–2_{02} and 4_{22}–3_{21}/4_{04}–3_{03} ratios (Fig. 5) might be caused by the para-H_2CO 3_{21}–2_{20}/3_{03}–2_{02} ratio bump (Fig. 4, top panel). This excitation effect in the para-H_2CO 3_{21}–2_{20}/3_{03}–2_{02} ratio may result in an overestimate of the kinetic temperature derived from this ratio with large uncertainty ($\gtrsim$20% at kinetic temperature >60 K) at spatial density $10^{5.5-7.0}$ cm^{-3}.

The para-H_2CO line intensity ratios 3_{22}–2_{21}/3_{03}–2_{02}, 3_{21}–2_{20}/3_{03}–2_{02}, 4_{23}–3_{22}/4_{04}–3_{03} and 4_{22}–3_{21}/4_{04}–3_{03} can also provide a measurement of the kinetic temperature of the gas assuming local thermodynamic equilibrium (LTE). The kinetic temperature can be calculated from these para-H_2CO transition ratios if the lines are optically thin (see Sect. 3.3) and originate from a high density region (Mangum & Wootten 1993). Following the method applied by Mangum & Wootten (1993) in their Appendix A,

$$T_{\rm LTE} = \frac{47.1}{\ln\left(0.556\frac{I(3_{03}-2_{02})}{I(3_{21}-2_{20})}\right)}\ {\rm K} \quad (1)$$

and

$$T_{\rm LTE} = \frac{47.2}{\ln\left(0.750\frac{I(4_{04}-3_{03})}{I(4_{22}-3_{21})}\right)}\ {\rm K}, \quad (2)$$

where $I(3_{03}$–$2_{02})/I(3_{21}$–$2_{20})$ and $I(4_{04}$–$3_{03})/I(4_{22}$–$3_{21})$ are the para-H_2CO integrated intensity ratios. The results of the kinetic temperature calculations from the para-H_2CO 3_{03}–2_{02}/3_{21}–2_{20} and 4_{04}–3_{03}/4_{22}–3_{21} integrated intensity ratios are listed in Table A.6. If the assumption of optically thin emission is correct, the kinetic temperatures derived from this method have an uncertainty of $\lesssim$30% (Mangum & Wootten 1993). We also compared the kinetic temperatures derived from LTE and RADEX non-LTE calculations (see Fig. 5). It appears that $T_{\rm non\text{-}LTE}$ is consistently higher than $T_{\rm LTE}$ by $\lesssim$25%. This might be caused by the fact that at densities of $10^{6.5}$ cm^{-3} (see Sect. 3.5) thermalization is not yet reached (Mangum & Wootten 1993). Therefore, higher $T_{\rm kin}$ values are needed to compensate for this effect, leading to lower excitation temperatures, and to reproduce data.

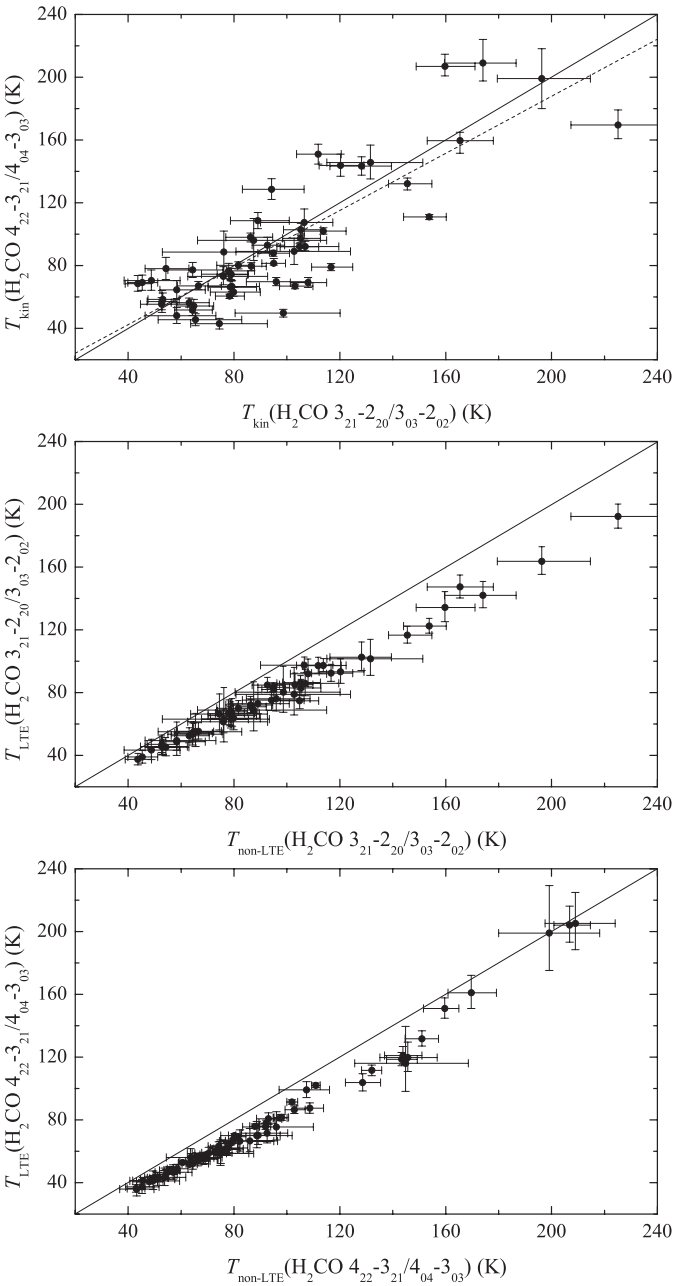

Fig. 5. *Top panel*: comparison of kinetic temperatures derived from para-H_2CO 3_{21}–2_{20}/3_{03}–2_{02} and 4_{22}–3_{21}/4_{04}–3_{03} ratios. The dashed line is the result from an unweighed linear fit, $T_{\rm kin}(4_{22}-3_{21}/4_{04}-3_{03}) = (0.9\pm0.1)\times T_{\rm kin}(3_{21}-2_{20}/3_{03}-2_{02}) + (5.8\pm7.8)$, with a correlation coefficient, R, of 0.85. *Middle and bottom panels*: comparisons of kinetic temperatures derived from LTE and RADEX non-LTE calculations for para-H_2CO 3_{21}–2_{20}/3_{03}–2_{02} and 4_{22}–3_{21}/4_{04}–3_{03} ratios, respectively. The temperature uncertainties are obtained from observed para-H_2CO line ratio errors. Solid lines indicate equal temperatures.

3.5. Spatial density and column density

As described in Sect. 1, with the kinetic temperature approximately known, the relative intensity ratio of H_2CO lines involving the same K_a ladders yields estimates of the spatial density of the gas (Henkel et al. 1980, 1983; Mangum & Wootten 1993).

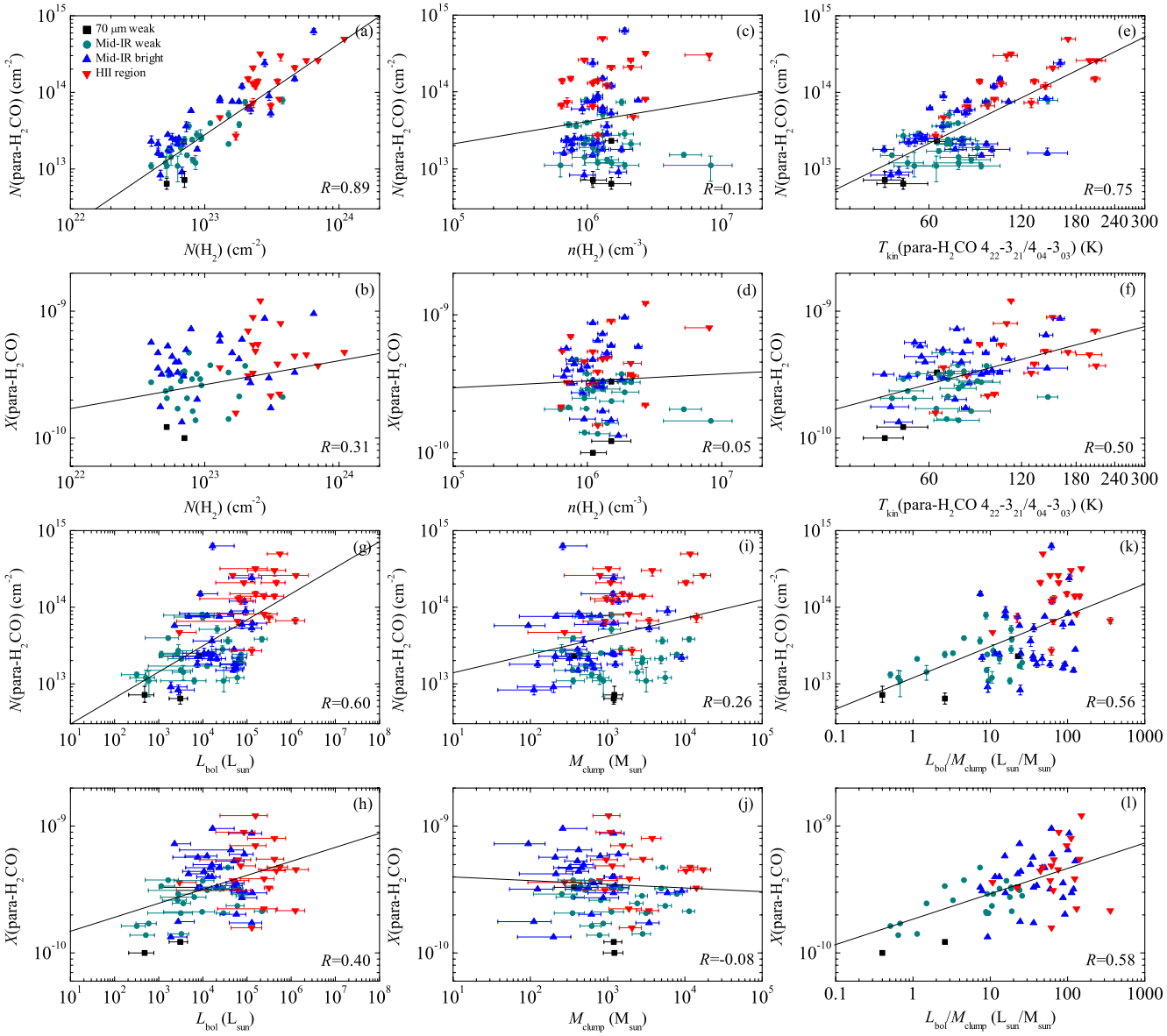

Fig. 6. Column density N(para-H_2CO) and fractional abundance X(para-H_2CO) vs. column density $N(H_2)$ (a, b), spatial density $n(H_2)$ (c, d), kinetic temperature T_{kin}(para-H_2CO 4_{22}–3_{21}/4_{04}–3_{03}) (e, f), bolometric luminosity (g, h), mass of clump (i, j), and luminosity-to-mass L_{bol}/M_{clump} ratio (k, l). The column density and spatial density uncertainties are obtained from observed para-H_2CO line brightness temperature and line ratio errors. The straight lines are the results from unweighed linear fits yielding the given correlation coefficients, R, in the lower right corner of each panel.

Table 3. Averaged parameters in various stages of the massive clumps.

Stage	T_{kin} K	$n(H_2)$ $\times 10^6$ cm^{-3}	N(para-H_2CO) $\times 10^{13}$ cm^{-2}	X(para-H_2CO) $\times 10^{-10}$	Δv(para-H_2CO 4_{04}–3_{03}) km s^{-1}
70w	52 ± 6	1.2 ± 0.2	1.2 ± 0.6	1.8 ± 0.7	3.9 ± 0.4
IRw	73 ± 4	1.7 ± 0.4	2.7 ± 0.4	2.7 ± 0.2	4.8 ± 0.2
IRb	81 ± 6	1.2 ± 0.1	7.2 ± 2.1	4.3 ± 0.4	4.9 ± 0.3
H II region	110 ± 8	1.8 ± 0.4	16.9 ± 0.3	4.9 ± 0.6	7.4 ± 0.4
Average	91 ± 4	1.5 ± 0.1	8.0 ± 1.3	3.9 ± 0.2	5.3 ± 0.2

For our observed transitions of H_2CO, para-H_2CO 4_{04}–3_{03}/3_{03}–2_{02}, 4_{22}–3_{21}/3_{21}–2_{20} (or 4_{22}–3_{21}/3_{22}–2_{21}), and 4_{23}–3_{22}/3_{22}–2_{21} (or 4_{23}–3_{22}/3_{21}–2_{20}) ratios are good densitometers to derive the spatial density. The para-H_2CO 3_{03}–2_{02} and 4_{04}–3_{03} lines are the strongest of the 218 GHz and 291 GHz transitions, respectively, and they are nearly all detected in our sample (see Table 2). Hence, we use the para-H_2CO 4_{04}–3_{03}/3_{03}–2_{02} integrated intensity ratio to derive the spatial density, which has also been used in molecular clouds of the Galactic CMZ (Immer et al. 2016).

We ran RADEX to obtain para-H_2CO column densities and spatial density, and calculated the observed para-H_2CO 3_{03}–2_{02} and 4_{04}–3_{03} integrated intensities in K km s^{-1} units corrected by the relevant beam-filling factors ($I \rightarrow I'$). In Fig. 3, an example is presented to show how the parameters are constrained by the corrected integrated line intensity and integrated line intensity ratio distribution of para-H_2CO in the N(para-H_2CO)–n(H_2) parameter space. This figure shows that at low column density (N(para-H_2CO) $< 5 \times 10^{14}$ cm^{-2}) the $I'(4_{04}$–$3_{03})/I'(3_{03}$–$2_{02})$ ratio accounting for different beam-filling factors (see the black solid lines) is sensitive to the gas spatial density and becomes relatively independent of the para-H_2CO column density, while the kinetic temperature is kept constant at ~55 K (which is close to the actual temperature; see above). At high column density (N(para-H_2CO) $> 5 \times 10^{14}$ cm^{-2}) the $I'(4_{04}$–$3_{03})/I'(3_{03}$–$2_{02})$ ratio does not appear to be sensitive to the gas spatial density and becomes dependent on the column density because the para-H_2CO 3_{03}–2_{02} transition starts to become optically thick (Mangum & Wootten 1993). The derived results of N(para-H_2CO) and spatial density are listed in Table A.6. We used the same method to obtain ortho-H_2CO column densities with the observed ortho-H_2CO (3_{12}–2_{11} and 3_{13}–2_{12}) integrated intensities, adopting kinetic temperature and spatial density derived from para-H_2CO line ratios (see Sect. 3.4 and above) and assuming ortho- and para-H_2CO originate from the same region. The obtained results of N(ortho-H_2CO) are listed in Table A.6.

As mentioned in Sect. 3.3, the para-H_2CO 3_{22}–2_{21}, 3_{21}–2_{20}, 4_{23}–3_{22}, and 4_{22}–3_{21} lines are optically thin, so the para-H_2CO 4_{22}–3_{21}/3_{21}–2_{20} (or 4_{23}–3_{22}/3_{22}–2_{21}) ratio is weakly affected by optical depths. To further check how optical depths influence the para-H_2CO 4_{04}–3_{03}/3_{03}–2_{02} ratio, we used the above method with the para-H_2CO 4_{22}–3_{21}/3_{21}–2_{20} ratio as well to constrain spatial density. The spatial densities obtained both from para-H_2CO 4_{04}–3_{03}/3_{03}–2_{02} (typical value ~1.0) and 4_{22}–3_{21}/3_{21}–2_{20} (typical value ~1.5) ratios yield similar values ($n(H_2) \sim 2 \times 10^6$ cm^{-3}), which confirms that para-H_2CO 3_{03}–2_{02} and 4_{04}–3_{03} lines are not strongly affected by saturation effects when trying to constrain spatial density and kinetic temperature in our sample. However, the ortho-H_2CO 3_{12}–2_{11} and 3_{13}–2_{12} lines are affected by opacities $\gtrsim 1$ in parts of our sample (see Sect. 3.3), so the N(ortho-H_2CO) may be underestimated in these sources.

The 870 μm continuum source angular sizes range from 22″ to 42″ with an average of 29″ in our sample. If the sizes of H_2CO are much smaller than those of the 870 μm continuum (and/or our beam size; see Table 1), the beam-filling factor is overestimated. If we assume that the H_2CO to 870 μm emission size ratio ($\theta_{H_2CO}/\theta_{870\,\mu m}$) is 90%, 80%, and 70%, for AGAL008.684−00.367 as an example (see Fig. 3), $n(H_2)$ decreases by 6%, 17%, and 23%. Mapping observations of massive clumps in CS (7-6) (Wu et al. 2010) and 350 μm continuum emission (Mueller et al. 2002) show that the median ratio of CS (7-6) emission size to the 350 μm continuum emission size is ~0.87 (Liu et al. 2016). Also considering the slightly different beam sizes for para-H_2CO 3_{03}–2_{02} and 4_{04}–3_{03} lines (see Sect. 3.2), we conclude that the beam-filling factor does not strongly influence our results for $n(H_2)$ constrained from para-H_2CO 4_{04}–3_{03}/3_{03}–2_{02} line ratios.

The statistical weight ratio of ortho- and para-H_2CO and previous H_2CO observations in other star-forming regions suggest that the ortho-to-para H_2CO abundance ratio is $\lesssim 3$ (Kahane et al. 1984; Mangum & Wootten 1993; Dickens & Irvine 1999; Jørgensen et al. 2005; Guzmán et al. 2011). In most of our sample (~95%) the obtained ortho-to-para H_2CO abundance ratios (N(ortho-H_2CO)/N(para-H_2CO)) range from 1.0 to 3.0 with an unweighted average of 2.0 ± 0.1. Assuming that H_2CO is formed in and expelled from dust grain mantles, this ratio corresponds to a dust temperature of $\lesssim$20 K (Kahane et al. 1984; Dickens & Irvine 1999).

4. Discussion

4.1. Variations of spatial density and H_2CO abundance

The gas spatial densities, $n(H_2)$, derived from para-H_2CO 4_{04}–3_{03}/3_{03}–2_{02} ratios, range from 6.3×10^5 to 8.3×10^6 cm^{-3} with an unweighted average of $1.5\,(\pm0.1) \times 10^6$ cm^{-3} (Table A.6); these values agree with the results determined with para-H_2CO (5_{05}–4_{04}/3_{03}–2_{02} and 5_{24}–4_{23}/3_{22}–2_{21}) and ortho-H_2CO (4_{13}–4_{14}/3_{12}–3_{13}) ratios from other star-forming regions (Mangum & Wootten 1993; Hurt et al. 1996; McCauley et al. 2011; Lindberg et al. 2015). Mapping the same para-H_2CO transitions towards the Galactic CMZ clouds shows that the spatial density of the widespread warm gas is constrained to 10^4–10^6 cm^{-3} (Immer et al. 2016). The spatial densities derived from para-H_2CO line ratios in our massive clumps overlap with the values found for high density regions in the Galactic CMZ clouds (see Table A.6 or Fig. 6, and Fig. 3 in Immer et al. 2016). The spatial density deduced from the dust indicates 10^3–10^6 cm^{-3} in our sample (Giannetti et al. 2017), which is lower than the spatial densities that we obtained. This suggests that H_2CO ($J = 3$–2 and 4–3) traces denser gas than the dust emission.

We derived unweighted averaged spatial densities obtained from para-H_2CO ratios in sources representing four evolutionary stages consisting of 70 μm weak (70w), mid-infrared weak (IRw), and mid-infrared bright (IRb) sources as well as star-forming clouds with ultra-compact H II regions. The unweighted averaged spatial densities $n(H_2)$ are $1.2\,(\pm0.2) \times 10^6$, $1.7\,(\pm0.4) \times 10^6$, $1.2\,(\pm0.1) \times 10^6$ cm^{-3}, and $1.8\,(\pm0.4) \times 10^6$ cm^{-3} in 70w, IRw, IRb, and H II regions, respectively (see Table 3 or Fig. 7). It seems that the averaged spatial densities traced by the para-H_2CO 4_{04}–3_{03}/3_{03}–2_{02} ratios do not vary significantly with the evolutionary stage of clumps. This may indicate that the density structure does not evolve significantly as the star formation proceeds. It also suggests that the para-H_2CO 4_{04}–3_{03}/3_{03}–2_{02} ratio may be a good densitometer to trace the dense gas at various stages of massive star formation.

The N(para-H_2CO) value derived from the para-H_2CO 4_{04}–3_{03}/3_{03}–2_{02} ratio ranges from 6.4×10^{12} to 6.1×10^{14} cm^{-2} with an unweighted average of $8.0\,(\pm1.3) \times 10^{13}$ cm^{-2} (Table 3), which agrees with the results from other protostellar cores and star-forming regions (Mangum & Wootten 1993; Hurt et al. 1996; Watanabe & Mitchell 2008; Tang et al. 2017a). We also derive averaged column densities of para-H_2CO for the four evolutionary stages mentioned above. The unweighted average column densities N(para-H_2CO) are $1.2\,(\pm0.6) \times 10^{13}$, $2.7\,(\pm0.4) \times 10^{13}$, $7.2\,(\pm2.1) \times 10^{13}$, and $16.9\,(\pm0.3) \times 10^{13}$ cm^{-2} in 70w, IRw, IRb, and H II regions, respectively (see

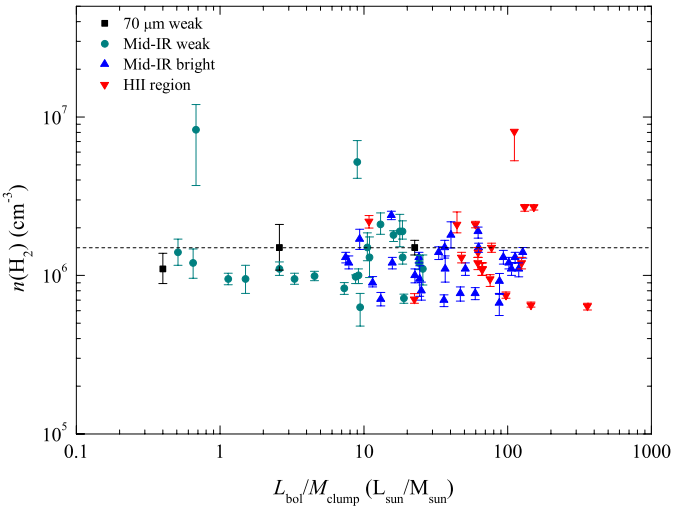

Fig. 7. Spatial density derived from para-H_2CO (4_{04}–3_{03}/3_{03}–2_{02}) vs. luminosity-to-mass ratio L_{bol}/M_{clump}. The dashed line indicates the average spatial density.

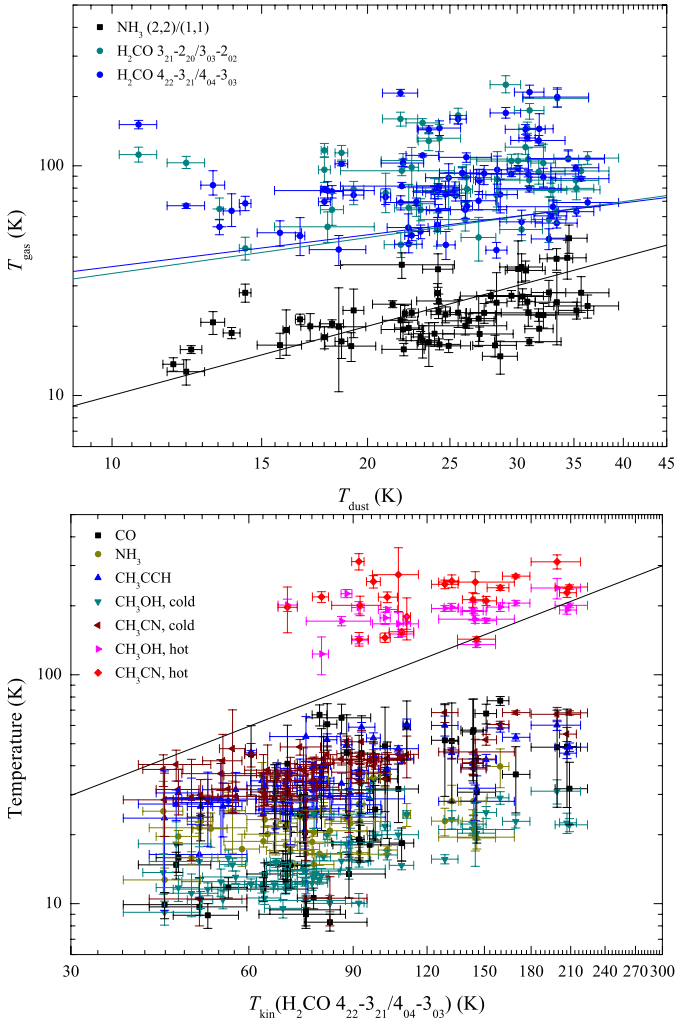

Fig. 8. *Top panel*: comparison of kinetic temperatures derived from para-H_2CO (3_{21}–2_{20}/3_{03}–2_{02} and 4_{22}–3_{21}/4_{04}–3_{03}, cyan and blue points) and NH_3 (2, 2)/(1, 1) (black squares) ratios against the dust temperatures. NH_3 kinetic temperatures are selected from Wienen et al. (2012). The cyan and blue straight lines are the results from unweighed linear fits for gas temperatures derived from para-H_2CO (3_{21}–2_{20}/3_{03}–2_{02} and 4_{22}–3_{21}/4_{04}–3_{03}, respectively. *Bottom panel*: comparisons of gas temperatures derived from para-H_2CO (4_{22}–3_{21}/4_{04}–3_{03}), CO, NH_3 (2, 2)/(1, 1), CH_3OH, CH_3CN, and CH_3CCH. Temperatures of CO, CH_3OH, CH_3CN, and CH_3CCH are taken from Giannetti et al. (2017). The black straight lines in both panels indicate equal temperatures.

Table 3). The fractional abundance X(para-H_2CO) = N(para-H_2CO)/$N(H_2)$ becomes 1.0×10^{-10}–1.2×10^{-9} with an average of $3.9\,(\pm0.2)\times10^{-10}$, where $N(H_2)$ is derived from the 870 μm continuum emission assuming a dust absorption coefficient $\kappa_{870} = 1.85\,\mathrm{cm^2\,g^{-1}}$ at 870 μm and adopting the temperature obtained from the dust (König et al. 2017). Therefore the abundance also agrees with the values found in other star formation regions, Galactic centre clouds, and external galaxies (Güsten & Henkel 1983; Zylka et al. 1992; Ao et al. 2013; Gerner et al. 2014; Tang et al. 2017a,b). The unweighted average fractional abundances X(para-H_2CO) are $1.8\,(\pm0.7)\times10^{-10}$, $2.7\,(\pm0.2)\times10^{-10}$, $4.3\,(\pm0.4)\times10^{-10}$, and $4.9\,(\pm0.6)\times10^{-10}$ in 70w, IRw, IRb, and H II regions, respectively (see Table 3). Averaged variations of fractional abundances of X(para-H_2CO) in various stages of star formation amount to nearly a factor of 3, which agrees with observed results in other massive star formation regions (van der Tak et al. 2000a,b; Gerner et al. 2014; Tang et al. 2017a). Therefore, we confirm that H_2CO can be widely used as a probe to trace the dense gas without drastic changes in abundance during various stages of star formation.

The column densities of para-H_2CO and the fractional abundances of X(para-H_2CO) with corresponding H_2 column density, spatial density $n(H_2)$, kinetic temperature T_{kin}(para-H_2CO 4_{22}–3_{21}/4_{04}–3_{03}), bolometric luminosity, clump mass, and luminosity-to-mass (L_{bol}/M_{clump}) ratio are shown in Fig. 6. It is apparent that the para-H_2CO column density increases proportionally to the H_2 column density, gas kinetic temperature, bolometric luminosity, and L_{bol}/M_{clump} ratio in the massive clumps. The fractional abundance of X(para-H_2CO) remains stable with increasing H_2 column density, spatial density, and mass of clump (Fig. 6). Nevertheless, the scatter in X(para-H_2CO) amounts to 0.1–1.2×10^{-9}, i.e. to a factor of ~10. The stable (relative to other molecular species; e.g. Tang et al. 2017b) para-H_2CO fractional abundances as a function of $N(H_2)$ indicate that H_2CO is a reliable tracer of the H_2 column density.

The luminosity-to-mass ratio is a good evolutionary tracer for massive and dense cluster-progenitor clumps (Molinari et al. 2008, 2016; Liu et al. 2013; Ma et al. 2013; Giannetti et al. 2017). The fractional abundance of X(para-H_2CO) shows a weak increasing trend with kinetic temperature, bolometric luminosity, and L_{bol}/M_{clump} ratio (see Fig. 6). The H_2CO abundances seem to increase with the evolutionary stage of massive clumps. Similar trends were seen in the massive star formation regions studied by Gerner et al. (2014) and Immer et al. (2014). This indicates that H_2CO abundances may be enhanced by high temperature, infrared radiation, and clump evolution, which would support a scenario in which H_2CO is increasingly released from dust grains into the gas phase during the evolution of the star-forming region.

4.2. Comparison of kinetic temperatures derived from gas and dust

The gas kinetic temperatures derived from the para-H_2CO (3_{21}–2_{20}/3_{03}–2_{02} and 4_{22}–3_{21}/4_{04}–3_{03}) line ratios are rather warm, ranging from 43 to >300 K with an unweighted average of 91 ± 4 K; these values agree with the results measured with

H_2CO in other massive star-forming regions and Galactic centre clouds (Mangum & Wootten 1993; Hurt et al. 1996; Mangum et al. 1999; Watanabe & Mitchell 2008; Nagy et al. 2012; Ao et al. 2013; Ginsburg et al. 2016; Immer et al. 2016; Lu et al. 2017). Most of our clumps, including the detected 70 μm weak clumps, are very warm, which indicates that there is likely ongoing massive star formation in most of our sample. The average kinetic temperatures $T_{\rm kin}$ are high in early evolutionary stages of the clumps (70w and IRw) (see Table 3), which is consistent with previous observational results measured with para-H_2CO (3–2) in star-forming regions with outflows (Tang et al. 2017a). Sixteen sources of our sample in early evolutionary stages have been observed in SiO (2–1) and (5–4) (Csengeri et al. 2016) SiO emission is detected in all these sources. This indicates that the dense gas probed by H_2CO may be heated by an outflow or shock. Therefore, in early evolutionary stages of the clumps, para-H_2CO traces higher temperature gas that may be related to gas excited by star formation activities (e.g. outflows, shocks) (Tang et al. 2017a).

Parts of our sample have been measured in NH_3 (2, 2)/(1, 1) by Wienen et al. (2012). We compare gas kinetic temperatures derived from para-H_2CO and NH_3 (2, 2)/(1, 1) against dust temperatures in Fig. 8. This comparison shows that the gas temperatures determined from NH_3 (2, 2)/(1, 1) agree with the dust temperatures (also see Giannetti et al. 2017), but are lower than those derived from para-H_2CO (3_{21}–2_{20}/3_{03}–2_{02} and 4_{22}–3_{21}/4_{04}–3_{03}). Previous observations towards the Galactic CMZ, dense massive clumps, and star formation regions indicate that in many cases para-H_2CO (3_{21}–2_{20}/3_{03}–2_{02} and 4_{22}–3_{21}/4_{04}–3_{03}) traces a higher kinetic temperature than the NH_3 (2, 2)/(1, 1) transitions and dust (Ao et al. 2013; Ott et al. 2014; Ginsburg et al. 2016; Immer et al. 2016; Tang et al. 2017a, 2018). The difference is likely because the derived kinetic temperatures from NH_3 (2, 2)/(1, 1) may reflect an average temperature of cooler and more diffuse gas (Henkel et al. 1987; Ginsburg et al. 2016), while para-H_2CO (J = 3–2 and 4–3) ratios trace denser and hotter regions more directly associated with star formation activity (Tang et al. 2017a, 2018).

Temperatures towards our selected massive clumps have been measured with CO, CH_3OH, CH_3CN, and CH_3CCH (Giannetti et al. 2017). We compare gas kinetic temperatures derived from para-H_2CO (4_{22}–3_{21}/4_{04}–3_{03}), CO, CH_3OH, CH_3CN, and CH_3CCH in Fig. 8. It shows that the gas temperatures determined from para-H_2CO are higher than those derived from CO, CH_3OH (cold component), CH_3CN (cold component), and CH_3CCH, but are lower than those obtained from the CH_3OH and CH_3CN hot components. This indicates that para-H_2CO (J = 3–2 and 4–3) ratios may trace dense gas in layers intermediate between those of CH_3CCH and CH_3CN (hot component) and the latter are likely most closely related to recently formed massive stars.

The dust temperatures of our sample are obtained from spectral energy distribution (SED) fitting to *Herschel* HiGal data at 70, 160, 250, 350, and 500 μm and ATLASGAL data at 870 μm by König et al. (2017). The results are listed in Table A.1. The derived dust temperature range in our observed sources is 11–41 K with an unweighted average of 25 ± 7 K. Previous observations show that the temperatures derived from gas and dust are often in agreement in the active dense clumps of Galactic disk clouds (Dunham et al. 2010; Giannetti et al. 2013; Battersby et al. 2014), but do not agree in the Galactic CMZ (Güsten et al. 1981; Ao et al. 2013; Ott et al. 2014; Ginsburg et al. 2016; Immer et al. 2016; Lu et al. 2017). As in the CMZ, the gas kinetic temperatures derived from para-H_2CO show higher values than the dust temperature with no apparent correlation (correlation coefficient $R \sim 0.2$) between $T_{\rm dust}$ and $T_{\rm gas}$ (see Fig. 8).

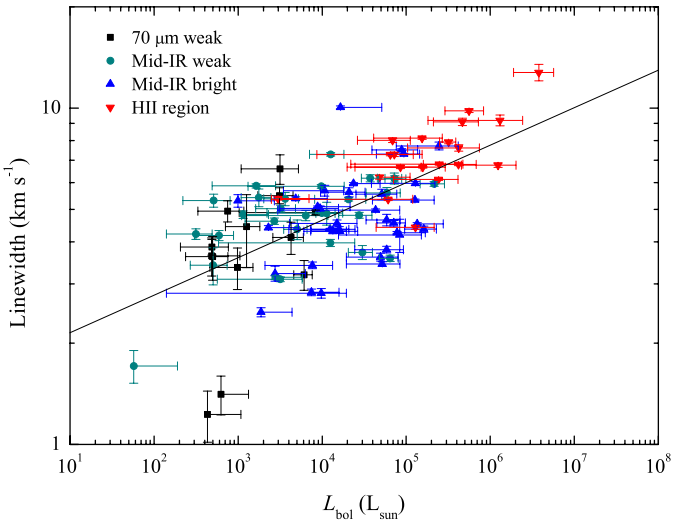

Fig. 9. Line width of the para-H_2CO (4_{04}–3_{03}) transition vs. bolometric luminosity of the measured sources. The straight line is the result from an unweighed linear fit.

It is commonly expected that the gas and dust are thermally coupled in the densest regions ($n(H_2) > 10^{4.5}$ cm^{-3}) (Goldsmith 2001) because at such densities interactions between dust and gas become sufficiently frequent. The dust emission at mid-infrared (MIR) emission traces primarily warm dust components (Helou 1986). Dust temperatures derived from MIR multi-filter data agree with gas temperatures derived from multi-inversion transitions of NH_3 in external galaxies (Melo et al. 2002; Tomono et al. 2006; Ao et al. 2011; Mauersberger et al. 2003). Combining the MIR data for our sample, the fit of the warm gas emission in the SED shows a cold and a warm component (see König et al. 2017). Our dust temperatures are taken from the cold component of the SED fitted results. Dust emission at far-infrared (FIR) emission originates primarily from colder dust components that may not be directly associated with star formation activity (Schnee et al. 2009; Bendo et al. 2012; Mangum et al. 2013a), therefore the dust temperatures derived from FIR measurements rarely exceed 50 K in star formation regions of our Galaxy and external galaxies (e.g. Henkel et al. 1986; Gao & Solomon 2004a; Bernard et al. 2010; Mangum et al. 2013a; Guzmán et al. 2015; Merello et al. 2015; He et al. 2016; Lin et al. 2016; König et al. 2017; Yu & Xu 2016; Tang et al. 2017a; Elia et al. 2017). This suggests that the HiGal dust emission may trace colder dust components that may not be used as a proxy for dust and gas kinetic temperatures (at least traced by H_2CO) in dense regions with massive star formation activity.

4.3. Line width-luminosity relation

The observed line widths of para-H_2CO (4_{04}–3_{03}) range from 1.2 to 12.8 km s^{-1} with an unweighted average of 5.3 ± 0.2 km s^{-1}. Using a mean unweighted kinetic temperature $T_{\rm kin} \sim 91$ K and averaged line widths of H_2CO, the thermal and non-thermal line widths are 0.15 and 2.25 km s^{-1}, respectively; $\sigma_{\rm T} = \sqrt{\frac{kT_{\rm kin}}{m_{\rm H_2CO}}}$ and $\sigma_{\rm NT} = \sqrt{\frac{\Delta v^2}{8\ln 2} - \sigma_{\rm T}^2}$, where k is the Boltzmann constant, $T_{\rm kin}$ is the kinetic temperature of the gas, $m_{\rm H_2CO}$ is the mass of the

formaldehyde molecule, and Δv is the measured FWHM line width of H_2CO. The thermal line width is significantly lower than the non-thermal line width. The sound speed ($a_s = \sqrt{\frac{kT_{kin}}{\mu m_H}}$, where $\mu = 2.37$ is the mean molecular weight for molecular clouds and m_H is the mass of the hydrogen atom) is $\sim 0.54\,km\,s^{-1}$ at temperature 91 K; hence, the Mach number (given as $M = \sigma_{NT}/a_s$) is 4.2, which agrees with the results of the high-mass clumps (mean value ~3.5 derived from NH_3; Wienen et al. 2012) and the Bolocam Galactic Plane Survey (BGPS) sources (mean value ~3.2 derived from NH_3; Dunham et al. 2011). This indicates that these massive clumps are turbulent and H_2CO line widths are influenced strongly by supersonic non-thermal motions in our samples.

Previous observations of NH_3 (Wouterloot et al. 1988; Myers et al. 1991; Harju et al. 1993; Ladd et al. 1994; Molinari et al. 1996; Jijina et al. 1999; Wu et al. 2006; Urquhart et al. 2011, 2015), $C^{18}O$ (Saito et al. 2001; Ridge et al. 2003; Maud et al. 2015), and ^{13}CO (Wang et al. 2009; Lundquist et al. 2015) suggest that the line width is correlated with luminosity, which indicates the presence of a link between formed stars and velocity dispersion. We investigate the line width-luminosity relation in the case of the dense gas tracer H_2CO. We plot the line width-luminosity relation in Fig. 9. For the line width of para-H_2CO (4_{04}–3_{03}) and bolometric luminosity, the least squares linear fit result is

$$\log \Delta v(H_2CO\ 4_{04}{-}3_{03}) = (0.11 \pm 0.01) \times \log L_{bol} + (0.23 \pm 0.06). \quad (3)$$

The correlation coefficient, R, is 0.64. Other transitions of H_2CO show similar $\Delta v(H_2CO)$–L_{bol} correlations (not shown here). The slope (0.11 ± 0.01) of the $\Delta v(H_2CO)$–L_{bol} correlation agrees with previous results found with $C^{18}O$ (Saito et al. 2001) and ^{13}CO (Wang et al. 2009), but is lower than that found with NH_3 (Wouterloot et al. 1988; Myers et al. 1991; Jijina et al. 1999; Wu et al. 2006; Urquhart et al. 2011, 2015). The correlation appears consistent with the idea that the internal velocity dispersion of the dense clumps can be used to determine the mass of the formed stars (Saito et al. 2001).

We also derive averaged line widths of para-H_2CO (4_{04}–3_{03}) discriminating between the four evolutionary stages introduced in Sect. 2. The unweighted averaged line widths are 3.9 ± 0.4, 4.8 ± 0.2, 4.9 ± 0.3, and $7.4 \pm 0.4\,km\,s^{-1}$ in 70w, IRw, IRb, and H II regions, respectively (see Table 3). It seems that the velocity dispersion slightly increases with the first three evolutionary stages, 70w, IRw, and IRb. A significant change appears to occur between the first three and the fourth (H II) evolutionary stage. This suggests that the more evolved and more luminous objects tend to be associated with more turbulent molecular cloud structures (Wang et al. 2009).

4.4. Non-thermal velocity dispersion-temperature relation

Previous observations of NH_3 and H_2CO (e.g. Wouterloot et al. 1988; Molinari et al. 1996; Jijina et al. 1999; Wu et al. 2006; Urquhart et al. 2011, 2015; Wienen et al. 2012; Lu et al. 2014; Immer et al. 2016; Tang et al. 2018) suggest that the line width is correlated with kinetic temperature. It is suggested that the correlation between kinetic temperature and line width is due to a conversion of turbulent energy into heat in the Galactic central clouds (e.g. Güsten et al. 1985; Ginsburg et al. 2016; Immer et al. 2016).

Here we examine whether there is a relationship between turbulence and temperature in our massive clumps. We adopt the non-thermal velocity dispersion (σ_{NT}) of para-H_2CO in good approximation as proxy for the turbulence, and the kinetic temperatures of para-H_2CO (3_{21}–$2_{20}/3_{03}$–2_{02} and 4_{22}–$3_{21}/4_{04}$–3_{03}) as the gas kinetic temperature (see Fig. 10). For the non-thermal velocity dispersion of para-H_2CO and kinetic temperature, the least squares linear fit results are listed in Table 4. The non-thermal velocity dispersion of para-H_2CO is significantly positively correlated with the gas kinetic temperature by a power law of the form $T_{kin} \propto \sigma_{NT}^{0.66-1.06}$, which is consistent with results found with NH_3 and H_2CO in other star formation regions (Wouterloot et al. 1988; Molinari et al. 1996; Jijina et al. 1999; Wu et al. 2006; Urquhart et al. 2011, 2015; Wienen et al. 2012; Lu et al. 2014; Tang et al. 2018). The gas is heated by turbulent energy according to the approximate relation $T_{kin} \propto \Delta v^{0.8-1.0}$ (gas kinetic temperature measured with NH_3 and H_2CO) in molecular clouds of the Galactic centre (Güsten et al. 1985; Mauersberger et al. 1987; Immer et al. 2016), which is consistent with our result (only in terms of slope, not of intercept and absolute value). All this implies that the gas may be heated by turbulent motions in our massive clumps on scales of ~0.1–1.8 pc.

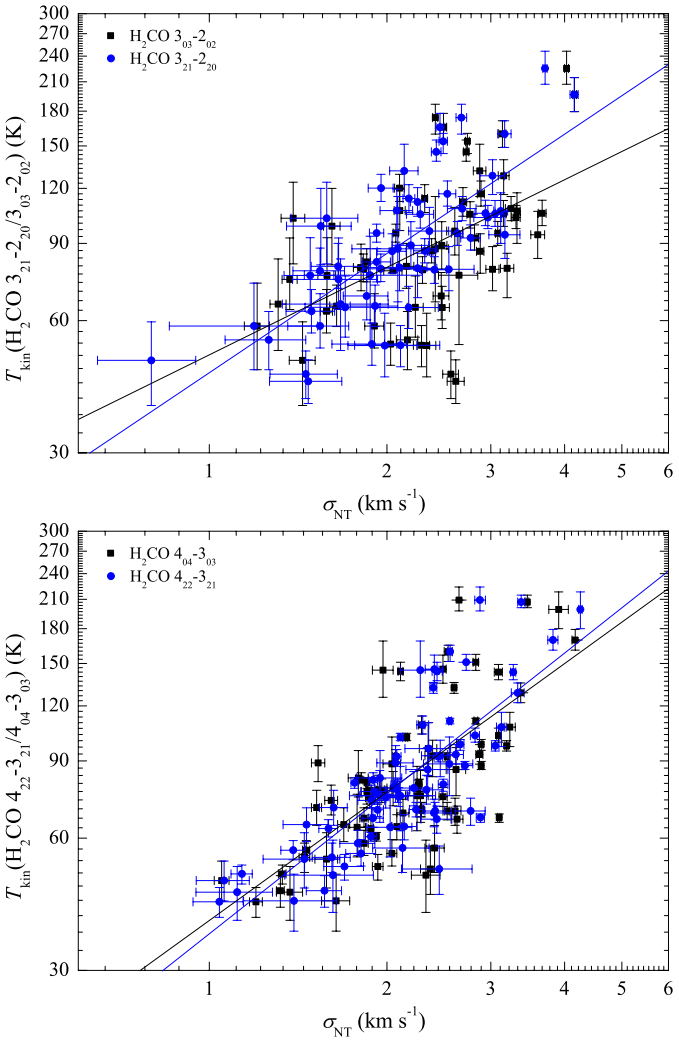

Fig. 10. Non-thermal velocity dispersion (σ_{NT}) vs. gas kinetic temperature for para-H_2CO. *Top panel*: gas kinetic temperatures were derived from para-H_2CO 3_{21}–$2_{20}/3_{03}$–2_{02} line ratios. *Bottom panel*: gas kinetic temperatures were derived from para-H_2CO 4_{22}–$3_{21}/4_{04}$–3_{03} line ratios. The straight lines are results from unweighed linear fits.

Table 4. Kinetic temperature vs. H_2CO non-thermal velocity dispersion.

Transition	T_{kin}–$\sigma_{NT}(H_2CO)$		
	Slope	Intercept	R
p-H_2CO 3_{03}–2_{02}	0.66 (0.15)	1.70 (0.06)	0.52
p-H_2CO 3_{21}–2_{20}	0.90 (0.11)	1.66 (0.04)	0.73
p-H_2CO 4_{04}–3_{03}	0.97 (0.12)	1.59 (0.04)	0.70
p-H_2CO 4_{22}–3_{21}	1.06 (0.10)	1.56 (0.04)	0.78

Notes. The format of the regression fits is $\log T_{kin}$ = Slope × $\log \sigma_{NT}(H_2CO)$ + Intercept. The value R is the correlation coefficient for the linear fit.

Recent para-H_2CO mapping observations of molecular clouds in the Galactic CMZ show that the warm dense gas is heated most likely by turbulence (Ao et al. 2013; Ginsburg et al. 2016; Immer et al. 2016). Following the method applied by Tang et al. (2018) in their Eq. (2),

$$3.3\times10^{-27}\, n\, \sigma_{NT}^{3}\, L^{-1} = 4\times10^{-33}\, n^{2}\, T_{turb}^{1/2}(T_{turb}-T_{dust}) + 6\times10^{-29}\, n^{1/2}\, T_{turb}^{3}\, \mathrm{d}v/\mathrm{d}r, \quad (4)$$

where the gas density n is in units of cm^{-3}, the velocity gradient dv/dr is in units of km s^{-1} pc^{-1}, the one-dimensional non-thermal velocity dispersion σ_{NT} is in units of km s^{-1}, and the cloud size L is in units of pc; we determined the gas kinetic temperature caused by turbulent energy. We computed the gas kinetic temperature assuming turbulent heating dominates the heating process. We assumed a cloud size of ~1 pc (e.g. Dunham et al. 2010, 2011; Rosolowsky et al. 2010; Urquhart et al. 2014; He et al. 2015; Wienen et al. 2015; König et al. 2017; Yuan et al. 2017), a velocity gradient $dv/dr = 1$ km s^{-1} pc^{-1}, the above-mentioned (Sect. 4.3) averaged non-thermal velocity dispersion of 2.25 km s^{-1} measured with H_2CO, and an averaged gas spatial density ~10^6 cm^{-3} derived from H_2CO line intensity ratios (Sect. 3.5). If the averaged dust temperature (T_{dust} ~ 25 K; derived from HiGal and ATLASGAL data; see Sect. 4.2) and averaged gas temperature (T_{kin} ~ 91 K; derived from the para-H_2CO line ratios; see Sect. 4.2) are adopted as the dust temperatures, the gas kinetic temperatures due to turbulence motions T_{turb}, are 55 and 88 K, respectively. The obtained T_{turb} values are slightly lower than the averaged gas kinetic temperature (T_{kin} ~ 91 K) derived from the para-H_2CO line ratios. This indicates that turbulent heating significantly contributes to gas temperature in these massive clumps on scales of ~0.1–1.8 pc, which agrees with previous observational results with H_2CO in the Orion molecular cloud 1 (OMC-1; Tang et al. 2018). Apparently, turbulent heating plays an important role in heating the dense gas in massive star-forming clumps (Pan & Padoan 2009).

4.5. Correlation of gas temperature with luminosity

Previous observations of our selected massive clump temperatures determined from CO, NH_3, CH_3CN, CH_3CCH, and CH_3OH (Wienen et al. 2012; Giannetti et al. 2014, 2017) suggest that these clumps are heated by radiation from internal massive stars. The comparison between the kinetic temperature and luminosity further helps us to understand the internal heating of embedded infrared sources upon their surrounding dense gas.

To investigate how the kinetic temperatures traced by para-H_2CO correlate with luminosity in these massive clumps, we compared the gas kinetic temperature to the bolometric luminosity obtained from MSX, WISE, *Herschel* HiGal and ATLASGAL data (König et al. 2017). A comparison between gas kinetic temperatures derived from para-H_2CO (3_{21}–2_{20}/3_{03}–2_{02} and 4_{22}–3_{21}/4_{04}–3_{03}) and the bolometric luminosity is shown in Fig. 11. The least squares linear fit results are

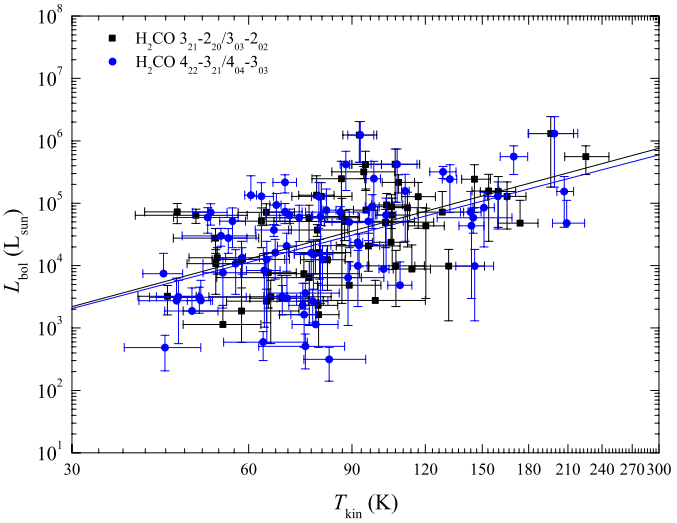

Fig. 11. Kinetic temperatures derived from para-H_2CO (3_{21}–2_{20}/3_{03}–2_{02} and 4_{22}–3_{21}/4_{04}–3_{03}, black squares and blue points) vs. bolometric luminosity. The straight lines are the results from unweighed linear fits.

$$\log L_{bol} = (2.53\pm0.54)\times\log T_{kin}(3_{21}-2_{20}/3_{03}-2_{02}) - (0.39\pm1.06) \quad (5)$$

and

$$\log L_{bol} = (2.46\pm0.52)\times\log T_{kin}(4_{22}-3_{21}/4_{04}-3_{03}) - (0.32\pm0.99), \quad (6)$$

with correlation coefficients, R, of 0.53 and 0.50, respectively. This shows that higher temperatures traced by H_2CO are associated with more luminous sources. This result is expected if dense gas probed by H_2CO is illuminated or heated by massive stars inside or adjacent to the clouds. The correlations between gas temperature and bolometric luminosity are weak. The bolometric luminosity and gas temperature derived from para-H_2CO are related by a power law of the form $L_{bol} \propto T_{kin}^{2.5\pm0.5}$, where the power-law index is not very far from that of the Stefan–Boltzmann law ($L \propto T_{kin}^{4}$). This also suggests that the dense gas is heated most likely by activity from associated massive stars.

Mapping NH_3 observations of massive star formation regions (Lu et al. 2014; Urquhart et al. 2015) shows that in some cases the gas is heated by radiation from external sources. Owing to a lack of H_2CO source structure information for our sample, we cannot exclude that external heating is contributing in some sources of our sample. Therefore, a detailed mapping study of the temperature structure of our structure using formaldehyde is needed. We intend to map a part of our sample with formaldehyde to reveal details of the gas heating mechanism in the future.

4.6. Gas temperature and clump evolution

To investigate whether the kinetic temperatures traced by para-H_2CO are influenced by massive young stellar objects (YSOs) at different evolutionary stages, we derived averaged kinetic

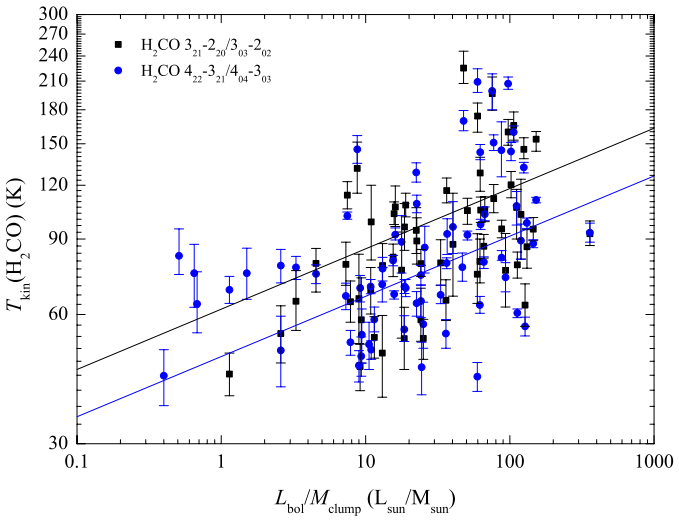

Fig. 12. Kinetic temperatures derived from para-H_2CO (3_{21}–2_{20}/3_{03}–2_{02} and 4_{22}–3_{21}/4_{04}–3_{03}, black squares and blue points) vs. luminosity-to-mass ratio L_{bol}/M_{clump}. The straight lines are the results from unweighed linear fits for clumps with $L_{bol}/M_{clump} \gtrsim 10\,L_{\odot}/M_{\odot}$.

temperatures obtained from the para-H_2CO (4_{22}–3_{21}/4_{04}–3_{03}) ratios for the four evolutionary stages outlined in Sect. 2. The unweighted average kinetic temperatures T_{kin} are 52 ± 6, 73 ± 4, 81 ± 6, and 110 ± 8 K in 70w, IRw, IRb, and H II regions, respectively (see Table 3). From this it is clear that the averaged gas kinetic temperature increases with the evolutionary stage, which confirms the trends measured with CO, NH_3, CH_3CN, CH_3CCH, CH_3OH, and dust emission in our sample and in other massive star-forming clumps (Giannetti et al. 2014, 2017; Guzmán et al. 2015; Molinari et al. 2016; He et al. 2016; Yu & Xu 2016; König et al. 2017; Yuan et al. 2017; Elia et al. 2017). This indicates that the gas temperature probed by para-H_2CO is related to the evolution of the clumps.

As mentioned in Sect. 4.1, the luminosity-to-mass ratio, L_{bol}/M_{clump}, is a good evolutionary tracer for massive and dense cluster-progenitor clumps, which defines a continuous evolutionary sequence in time. We plot the relation between kinetic temperature derived from para-H_2CO (3_{21}–2_{20}/3_{03}–2_{02} and 4_{22}–3_{21}/4_{04}–3_{03}) ratios and L_{bol}/M_{clump} ratios in Fig. 12. The plot shows that the kinetic temperature traced by para-H_2CO is indeed a rising function of the luminosity-to-mass ratio, which is consistent with results found from CH_3CN, CH_3CCH, and CH_3OH in massive star-forming clumps (Molinari et al. 2016; Giannetti et al. 2017).

It seems that massive stars reach the main sequence above a threshold of $L_{bol}/M_{clump} \sim 10\,L_{\odot}/M_{\odot}$ (Giannetti et al. 2017), thus strongly increasing their energy output. The $L_{bol}/M_{clump} \gtrsim 10\,L_{\odot}/M_{\odot}$ clumps are associated with IRb and H II regions in our sample (also see Giannetti et al. 2017), indicating late evolutionary stages (see Table A.1). For $L_{bol}/M_{clump} \gtrsim 10\,L_{\odot}/M_{\odot}$, the gas temperature and the luminosity-to-mass ratio are related by power laws of the form

$$\log T_{kin}(3_{21}\text{–}2_{20}/3_{03}\text{–}2_{02}) = (0.14 \pm 0.05) \times \log(L_{bol}/M_{clump}) + (1.79 \pm 0.09) \quad (7)$$

and

$$\log T_{kin}(4_{22}\text{–}3_{21}/4_{04}\text{–}3_{03}) = (0.16 \pm 0.04) \times \log(L_{bol}/M_{clump}) + (1.68 \pm 0.08), \quad (8)$$

with correlation coefficients, R, of 0.37 and 0.45, respectively. The power-law indices are consistent with those derived from CH_3CN, CH_3CCH, and CH_3OH in our and other massive clumps ($T \propto (L_{bol}/M_{clump})^{0.12-0.22}$, Molinari et al. 2016; Giannetti et al. 2017). A correlation between gas temperature and L_{bol}/M_{clump} ratio indicates that the dense gas appears to be heated by the newly formed massive stars during the late evolutionary stages of clumps. The $L_{bol}/M_{clump} < 10\,L_{\odot}/M_{\odot}$ clumps are well associated with 70w and IRw indicating earlier evolutionary stages. For these sources the relation of gas temperature with the L_{bol}/M_{clump} ratio does not follow the above trend. The temperature in these sources may not yet be greatly affected by the gas that is heated by internal power sources (Molinari et al. 2016). Instead it may be related to gas excited by star formation activities, such as outflows and shocks (Tang et al. 2017a).

4.7. Comparisons of H_2CO luminosity, bolometric luminosity, and clump mass

The line luminosities of dense molecular gas tracers (e.g. HCN, CS, and HCO^+) are found to be approximately linearly correlated with far-infrared luminosities ($L_{FIR} \propto L_{molecule}$) in both Galactic dense clumps and galaxies (Gao & Solomon 2004a,b; Wu et al. 2005, 2010; Schenck et al. 2011; Ma et al. 2013; Zhang et al. 2014; Liu et al. 2016; Stephens et al. 2016), which indicates a link between the SFR represented by infrared luminosities and dense molecular gas mass indicated by molecular line luminosities. Line luminosities of dense molecular gas (e.g. HCN, CS, HCO^+, N_2H^+, SO) appear to be linearly related to the mass of dense gas most relevant to star formation (Wu et al. 2010; Reiter et al. 2011; Liu et al. 2016).

Observations of H_2CO K-doublet transitions ($\Delta J = 0$, $\Delta K_a = 0$, $\Delta K_c = \pm 1$) in our Galaxy and external galaxies show that H_2CO traces a denser, more compact component of molecular clouds than low-excitation transitions of CO or HCN (Mangum et al. 1993, 2008, 2013b). Our selected H_2CO transitions may have similar characteristics. The critical densities of H_2CO 3_{13}–2_{12}, 3_{12}–2_{11}, 3_{03}–2_{02}, and 4_{04}–3_{03} transitions are $\sim 4 \times 10^5$, $\sim 6 \times 10^5$, $\sim 6 \times 10^5$, and $\sim 1 \times 10^6$ cm^{-3} (at kinetic temperature 50 K; Shirley 2015), respectively. Following Wu et al. (2005) and assuming Gaussian brightness distributions for the sources and a Gaussian beam, H_2CO line luminosities L'_{H_2CO} can be derived with

$$L'_{H_2CO} = 23.5 \times 10^{-6} \times D^2 \times \left(\frac{\pi \times \theta_s^2}{4 \ln 2}\right) \times \left(\frac{\theta_s^2 + \theta_{beam}^2}{\theta_s^2}\right) \times \int T_{mb} dV. \quad (9)$$

Here D is the distance in kpc from König et al. (2017), and θ_s and θ_{beam} are the sizes of the line emission source and of the beam in arcsecond. As described in Sect. 3.5, we assume that the extent of the H_2CO emission is the same as that of the 870 μm dust emission derived from Csengeri et al. (2014). The resulting L'_{H_2CO} values are listed in Table A.7.

We present the correlations between clump masses and H_2CO luminosities in Fig. 13. The power-law fitted results are listed in Table 5. These show that the M_{clump}–L'_{H_2CO} relations are strongly correlated and that correlation coefficients range from 0.84 to 0.93 for various H_2CO transitions. The power-law correlations of M_{clump}–L'_{H_2CO} are found to be slightly sublinear and are consistent with results of, for example HCN, CS, HCO^+, N_2H^+, and SO found in massive dense clumps (Wu et al. 2010; Reiter et al. 2011; Liu et al. 2016). This indicates that L'_{H_2CO} of our

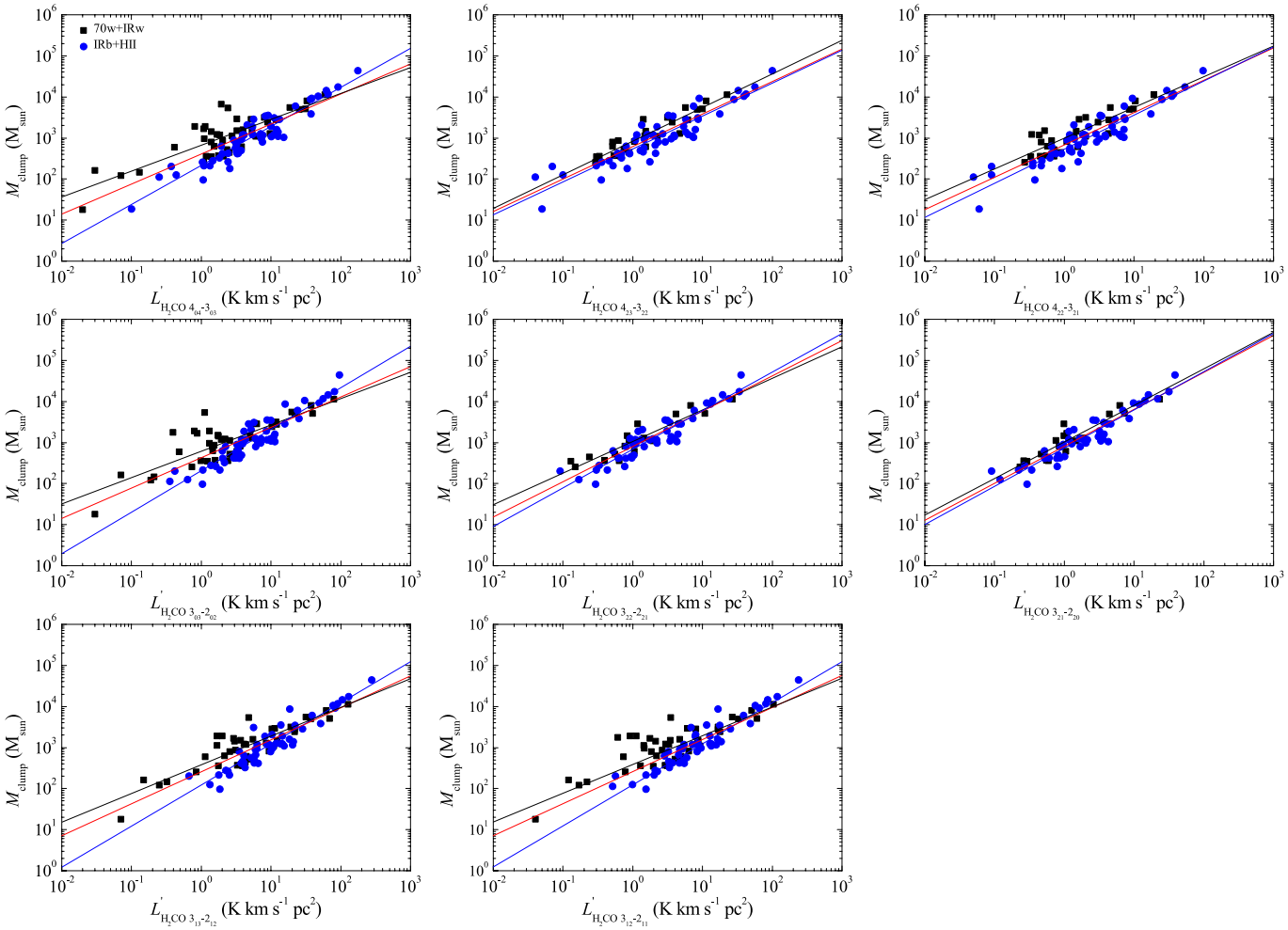

Fig. 13. M_{clump} vs. L'_{H_2CO} for eight transition lines of H_2CO. Black squares indicate clumps classified as early stage (70w and IRw) and blue circles indicate clumps classified as late stage (IRb and H II regions) (see Sect. 2 for an introduction to these sources). The black, blue, and red lines are the results from linear fits for early stage, late stage, and all sources, respectively.

observed eight transitions provides good tracers for the mass of dense gas and confirms that $L'_{molecule}$ of dense molecular tracers does reliably probe the mass of dense molecular gas.

The L_{bol}–L'_{H_2CO} relations are plotted in Fig. 14. We fit power-law relations of L_{bol}–L'_{H_2CO} for eight different H_2CO transitions. The fitted results are listed in Table 5. The bolometric luminosities and the H_2CO luminosities are related with a slope range of 0.98–1.19 and correlation coefficients ranging from 0.79 to 0.82 for different H_2CO transitions. Considering the uncertainties, the correlations are nearly linear. The correlations of L_{bol}–L'_{H_2CO} for different H_2CO transitions are consistent with previous observational results of, for example, HCN, CS, HCO^+, SiO, HC_3N, C_2H in massive dense clumps (Wu et al. 2005, 2010; Ma et al. 2013; Liu et al. 2016; Stephens et al. 2016). This indicates that the mass of dense molecular gas traced by the H_2CO line luminosity is well correlated with star formation.

Observations of dense clumps show that their evolutionary stage impacts the L_{IR}–$L'_{molecule}$ relation (Liu et al. 2016; Stephens et al. 2016). We distinguish two evolutionary classes of clumps in their early stage (70w and IRb) and late stage (IRb and H II regions), respectively, in Fig. 14, and the power-law fitted results are listed in Table 5. Considering uncertainties of the fitted slopes of L_{bol}–L'_{H_2CO} correlations, we find approximately similar linear correlations of L_{bol}–L'_{H_2CO} for various transitions in both evolutionary stages of the clumps. This suggests that the L_{IR}–L'_{H_2CO} relations are only weakly influenced by the evolutionary stage of the clumps in our sample. We also compare the M_{clump}–L'_{H_2CO} relations in the two evolutionary stages in Fig. 13, and the power-law fitted results are listed in Table 5. Apparently, clumps in an early stage are closer to sublinear (slopes of 0.63–0.89) and clumps in a late stage tend to exhibit more linear slopes (0.80–1.01). For the early stage, the M_{clump}–L'_{H_2CO} data show a larger scatter (see Fig. 13). This may be due to some clumps with lower luminosity ($<10^3\ L_\odot$), which are likely in an early evolutionary stage with large derived uncertainties of the mass of the clump. The M_{clump}–L'_{H_2CO} is found to be strongly correlated, with correlation coefficients ranging from 0.92 to 0.94 in the late stages of clumps. This indicates that L'_{H_2CO} ($J = 3$–2 and 4–3) traces well the mass of warm dense molecular gas associated with bright infrared emission and H II regions in massive star-forming clumps.

5. Summary

We have measured the kinetic temperature and spatial density with H_2CO ($J = 4$–3) and (3–2) rotational transitions and compare the derived temperatures with values obtained from NH_3

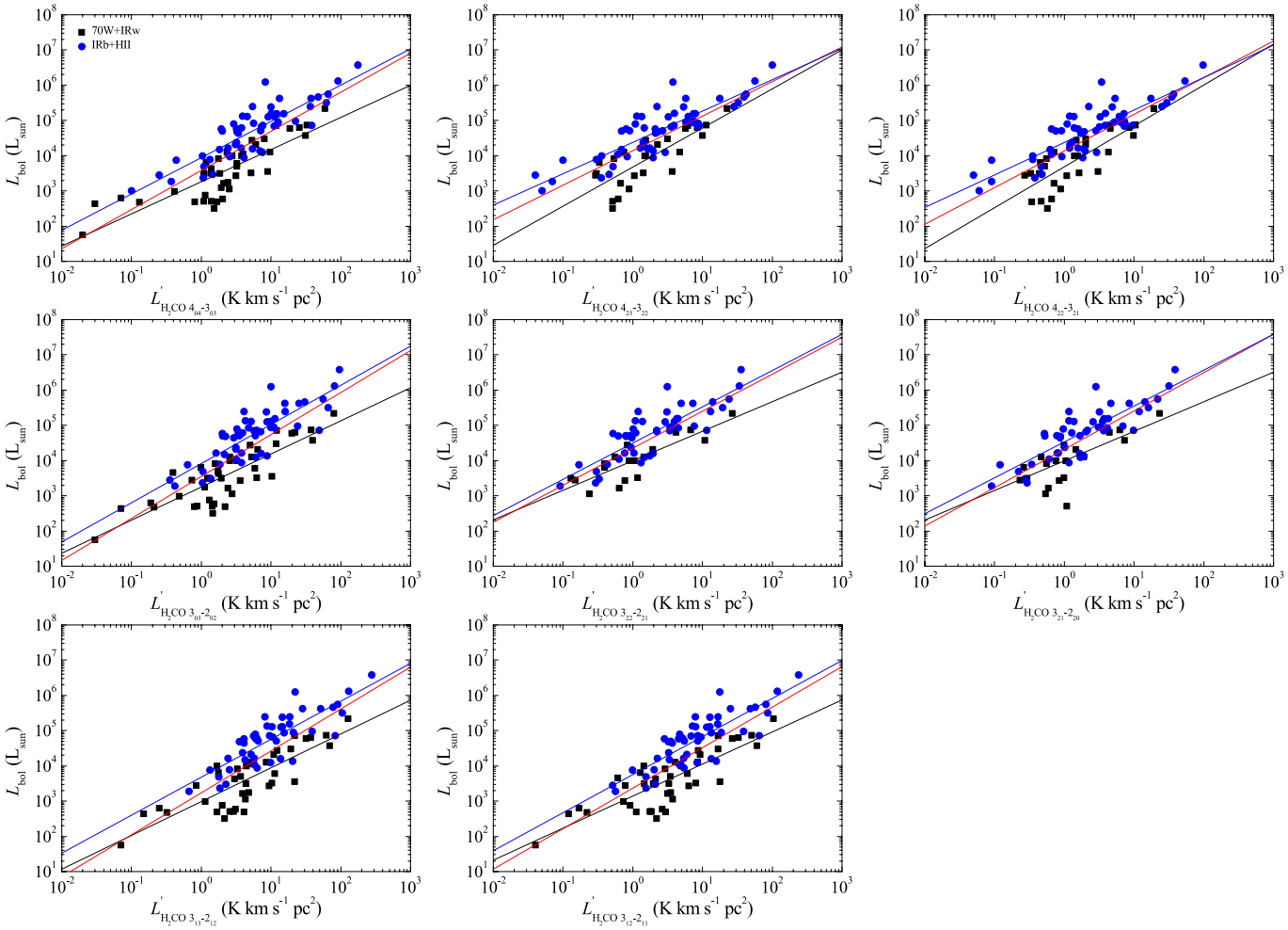

Fig. 14. L_{bol} vs. L'_{H_2CO} for eight transition lines of H_2CO. Black squares indicate clumps classified as early stage (70w and IRw) and blue circles indicate clumps classified as late stage (IRb and H II regions). The black, blue, and red lines are the results from linear fits for early stage, late stage, and all sources, respectively.

with dust emission, line width, and bolometric luminosity for the ATLASGAL TOP100 massive star-forming clumps at various evolutionary stages using the 12 m APEX telescope. The main results are the following:

Using the RADEX non-LTE model, we derived the gas kinetic temperature and spatial density, modelling the measured para-H_2CO 3_{21}–2_{20}/3_{03}–2_{02}, 4_{22}–3_{21}/4_{04}–3_{03}, and 4_{04}–3_{03}/3_{03}–2_{02} ratios. The gas kinetic temperatures derived from the para-H_2CO 4_{22}–3_{21}/4_{04}–3_{03} and 3_{21}–2_{20}/3_{03}–2_{02} line ratios are very warm, ranging from 43 to >300 K with an unweighted average of 91 ± 4 K. Spatial densities of molecular gas derived from the para-H_2CO 4_{04}–3_{03}/3_{03}–2_{02} line ratios yield 0.6–8.3 × 10^6 cm^{-3} with an unweighted average of 1.5 (±0.1) × 10^6 cm^{-3}.

The fractional abundance X(para-H_2CO) does not vary considerably during the various stages of massive star formation, ranging from 1.0×10^{-10} to 1.2×10^{-9} with an average of $3.9\,(\pm0.2) \times 10^{-10}$, confirming that H_2CO does reliably trace the H_2 column density.

The spatial densities traced by H_2CO do not vary significantly with the evolutionary stage of massive clumps. This may indicate that the density structure does not evolve significantly as the star formation proceeds.

A comparison of kinetic temperatures derived from para-H_2CO, NH_3 (2, 2)/(1, 1), and the dust emission indicates that para-H_2CO traces a distinctly higher temperature than the NH_3 (2, 2)/(1, 1) transitions and dust.

The H_2CO line widths correlate with the bolometric luminosities and increase with the evolutionary stage of the clumps, which suggests that high luminosities tend to be associated with more turbulent molecular cloud structures.

The non-thermal velocity dispersion of H_2CO is positively correlated with the gas kinetic temperature, which indicates that the dense gas may be heated by dissipation of turbulent energy in those massive clumps.

A weak positive correlation between gas temperature and bolometric luminosity suggests that the gas might be heated by the activity of the embedded young massive stars.

The average gas kinetic temperature clearly increases with the evolutionary stage of the massive clumps. For $L_{bol}/M_{clump} \gtrsim 10\,L_\odot/M_\odot$, we find a rough correlation between gas kinetic temperature and L_{bol}/M_{clump} ratio, which traces the evolutionary stage of the massive clumps (Molinari et al. 2016; Giannetti et al. 2017).

The strong correlations between H_2CO line luminosities and clump masses are approximately linear during the late evolutionary stages of clumps, which indicates that L_{H_2CO} (J = 3–2) and (4–3) reliably trace the mass of warm dense molecular gas associated with bright infrared emission and H II regions. During

Table 5. Clump mass and bolometric luminosity vs. H_2CO line luminosity.

Transition	Sample	M_{clump}–L'_{H_2CO}			L_{bol}–L'_{H_2CO}		
		Slope	Intercept	R	Slope	Intercept	R
o-H_2CO 3_{13}–2_{12}	70w+IRw	0.70 (0.06)	2.57 (0.06)	0.88	0.96 (0.11)	2.98 (0.10)	0.82
	IRb+H II	0.99 (0.05)	2.09 (0.06)	0.93	1.10 (0.10)	3.66 (0.12)	0.84
	all	0.78 (0.05)	2.40 (0.05)	0.88	1.19 (0.09)	3.24 (0.10)	0.80
o-H_2CO 3_{12}–2_{11}	70w+IRw	0.63 (0.07)	2.71 (0.06)	0.83	0.91 (0.10)	3.14 (0.09)	0.82
	IRb+H II	0.98 (0.05)	2.17 (0.06)	0.94	1.08 (0.10)	3.75 (0.11)	0.84
	all	0.72 (0.05)	2.53 (0.05)	0.84	1.16 (0.09)	3.37 (0.09)	0.81
p-H_2CO 3_{03}–2_{02}	70w+IRw	0.64 (0.07)	2.79 (0.06)	0.82	0.94 (0.10)	3.25 (0.08)	0.83
	IRb+H II	1.01 (0.06)	2.32 (0.05)	0.93	1.11 (0.11)	3.92 (0.10)	0.83
	all	0.74 (0.05)	2.63 (0.04)	0.84	1.19 (0.09)	3.55 (0.08)	0.81
p-H_2CO 3_{22}–2_{21}	70w+IRw	0.77 (0.07)	3.02 (0.05)	0.93	0.84 (0.13)	3.99 (0.08)	0.85
	IRb+H II	0.94 (0.05)	2.84 (0.03)	0.94	1.03 (0.10)	4.49 (0.07)	0.83
	all	0.86 (0.04)	2.91 (0.03)	0.93	1.05 (0.09)	4.35 (0.06)	0.82
p-H_2CO 3_{21}–2_{20}	70w+IRw	0.89 (0.08)	3.01 (0.04)	0.93	0.95 (0.20)	3.90 (0.11)	0.75
	IRb+H II	0.93 (0.05)	2.86 (0.03)	0.94	1.02 (0.10)	4.51 (0.06)	0.84
	all	0.90 (0.04)	2.91 (0.03)	0.93	1.09 (0.11)	4.32 (0.07)	0.79
p-H_2CO 4_{04}–3_{03}	70w+IRw	0.63 (0.07)	2.82 (0.05)	0.83	0.91 (0.10)	3.26 (0.08)	0.83
	IRb+H II	0.95 (0.05)	2.33 (0.04)	0.94	1.03 (0.08)	3.95 (0.08)	0.86
	all	0.73 (0.05)	2.61 (0.04)	0.85	1.11 (0.08)	3.59 (0.07)	0.82
p-H_2CO 4_{23}–3_{22}	70w+IRw	0.82 (0.07)	2.92 (0.04)	0.93	1.11 (0.17)	3.67 (0.10)	0.80
	IRb+H II	0.80 (0.05)	2.73 (0.04)	0.92	0.89 (0.07)	4.38 (0.06)	0.86
	all	0.79 (0.04)	2.79 (0.03)	0.91	0.98 (0.09)	4.15 (0.06)	0.79
p-H_2CO 4_{22}–3_{21}	70w+IRw	0.75 (0.09)	2.99 (0.05)	0.86	1.16 (0.17)	3.68 (0.09)	0.80
	IRb+H II	0.83 (0.05)	2.73 (0.04)	0.92	0.92 (0.08)	4.38 (0.06)	0.86
	all	0.79 (0.05)	2.83 (0.03)	0.89	1.04 (0.09)	4.13 (0.06)	0.80

Notes. Format of the regression fits is $\log L_{bol}$ (or $\log M_{clump}$) = Slope × $\log L'_{H_2CO}$ + Intercept. The value R is the correlation coefficient for the linear fit.

the earlier evolutionary stages of clumps, the correlation may be slightly sublinear. The M_{clump}–L'_{H_2CO} correlation appears to be influenced by the evolutionary stage of the clumps.

The H_2CO line luminosities are nearly linearly correlated with bolometric luminosities over about four orders of magnitude in L_{bol} of our massive clumps, suggesting that the mass of dense molecular gas traced by the H_2CO line luminosity is well correlated with star formation. The L_{bol}–L'_{H_2CO} relation seems to be weakly affected by the evolutionary stage of the clumps.

Acknowledgements. The authors are grateful for the valuable comments of the referee Jeff Mangum. We thank the staff of the APEX telescope for their assistance in observations. We also thank Nina Brinkmann for her help with data calibration. This work acknowledges support by The National Natural Science Foundation of China under grant 11433008, The Program of the Light in China's Western Region (LCRW) under grant XBBS201424, and The National Natural Science Foundation of China under grant 11373062. This work was partially carried out within the Collaborative Research Council 956, subproject A6, funded by the Deutsche Forschungsgemeinschaft (DFG). C. H. acknowledges support by a Chinese Academy of Sciences President's International Fellowship Initiative for visiting scientists (2017VMA0005). This research has used NASA's Astrophysical Data System (ADS).

References

Ao, Y., Henkel, C., Braatz, J. A., et al. 2011, A&A, 529, A154
Ao, Y., Henkel, C., Menten, K. M., et al. 2013, A&A, 550, A135
Battersby, C., Bally, J., Dunham, M., Ginsburg, A., et al. 2014, ApJ, 786, 116
Bendo, G. J., Boselli, A., Dariush, A., et al. 2012, MNRAS, 419, 1833
Bernard, J.-Ph., Paradis, D., Marshall, D. J., et al. 2010, A&A, 518, L88
Bieging, J. H., Wilson, T. L., & Downes, D. 1982, A&AS, 49, 607
Contreras, Y., Schuller, F., Urquhart, J. S., et al. 2013, A&A, 549, A45
Csengeri, T., Urquhart, J. S., Schuller, F., et al. 2014, A&A, 565, A75
Csengeri, T., Leurini, S., Wyrowski, F., et al. 2016, A&A, 586, A149 (Paper II)
Dickens, J. E., & Irvine, W. M. 1999, ApJ, 518, 733
Downes, D., Wilson, T. L., Bieging, J., & Wink, J. 1980, A&AS, 40, 379
Dunham, M. K., Rosolowsky, E., Evans, N. J. II, et al. 2010, ApJ, 717, 1157
Dunham, M. K., Rosolowsky, E., Evans, N. J. II, et al. 2011, ApJ, 741, 110
Elia, D., Molinari, S., Schisano, E., et al. 2017, MNRAS, 471, 100
Gao, Y., & Solomon, P. M. 2004a, ApJ, 606, 271
Gao, Y., & Solomon, P. M. 2004b, ApJS, 152, 63
Gerner, T., Beuther, H., Semenov, D., et al. 2014, A&A, 563, A97
Giannetti, A., Brand, J., Sánchez-Monge, Á., et al. 2013, A&A, 556, A16
Giannetti, A., Wyrowski, F., Brand, J., et al. 2014, A&A, 570, A65 (Paper I)
Giannetti, A., Leurini, S., Wyrowski, F., et al. 2017, A&A, 603, A33 (Paper V)
Ginsburg, A., Darling, J., Battersby, C., et al. 2011, ApJ, 736, 149
Ginsburg, A., Bally, J., Battersby, C., et al. 2015, A&A, 573, A106
Ginsburg, A., Henkel, C., Ao, Y., Riquelme, D., et al. 2016, A&A, 586, A50
Ginsburg, A., Goddi, C., Kruijssen, J. D., et al. 2017, ApJ, 842, 92
Goldsmith, P. F. 2001, ApJ, 557, 736
Gong, Y., Henkel, C., Spezzano, S., et al. 2015a, A&A, 574, A56
Gong, Y., Henkel, C., Thorwirth, S., et al. 2015b, A&A, 581, A48
Guo, W. H., Esimbek, J., Tang, X. D., et al. 2016, Ap&SS, 361, 264
Güsten, R., & Henkel, C. 1983, A&A, 125, 136
Güsten, R., Walmsley, C. M., & Pauls, T. 1981, A&A, 103, 197
Güsten, R., Walmsley, C. M., Ungerechts, H., et al. 1985, A&A, 142, 381
Guzmán, V., Pety, J., Goicoechea, J. R., et al. 2011, A&A, 534, A49
Guzmán, A. E., Sanhueza, P., Contreras, Y., et al. 2015, ApJ, 815, 130
Harju, J., Walmsley, C. M., & Wouterloot, J. G. A. 1993, A&AS, 98, 51
He, Y. X., Zhou, J. J., Esimbek, J., et al. 2015, MNRAS, 450, 1926
He, Y. X., Zhou, J. J., Esimbek, J., et al. 2016, MNRAS, 461, 2288
Helou, G. 1986, ApJL, 311, L33
Henkel, C., Walmsley, C. M., & Wilson, T. L. 1980, A&A, 82, 41

Henkel, C., Wilson, T. L., Walmsley, C. M., & Pauls, T. 1983, A&A, 127, 388
Henkel, C., Wouterloot, J. G. A., & Bally, J. 1986, A&A, 155, 193
Henkel, C., Wilson, T. L., & Mauersberger, R. 1987, A&A, 182, 137
Henkel, C., Baan, W. A., & Mauersberger, R. 1991, A&ARv, 3, 47
Hurt, R., Barsony, M., & Wootten, A. 1996, ApJ, 456, 686
Immer, K., Galván-Madrid, R., König, C., et al. 2014, A&A, 572, A63
Immer, K, Kauffmann, J., Pillai, T., et al. 2016, A&A, 595, A94
Jijina, J., Myers, P. C., & Adams Fred, C. 1999, ApJS, 125, 161
Johnston, K. G., Beuther, H., Linz, H., et al. 2014, A&A, 568, A56
Johnstone, D., & Bally, J. 1999, ApJ, 510L, 49
Jørgensen, J. K., Schöier, F. L., & van Dishoeck, E. F. 2005, A&A, 437, 501
Kahane, C., Lucas, R., Frerking, M. A., et al. 1984, A&A, 137, 211
Kim, W. J., Wyrowski, F., Urquhart, J. S., et al. 2017, A&A, 602, A37 (Paper IV)
König, C., Urquhart, J. S., Csengeri, T., et al. 2017, A&A, 599, A139 (Paper III)
Ladd, E. F., Myers, P. C., & Goodman, A. A. 1994, ApJ, 433, 117
Lada, C. J., Lombardi, M., & Alves, J. F. 2010, ApJ, 724, 687
Lin, Y. X, Liu, H. B., Li, D., et al., 2016, ApJ, 828, 32
Lindberg, J. E., Jørgensen, J. K., Watanabe, Y., et al. 2015, A&A, 584, A28
Liu, T., Wu, Y., & Zhang, H. 2013, ApJ, 775L, 2
Liu, T., Kim, K., Yoo, H., et al. 2016, ApJ, 829, 59
Lu, X., Zhang, Q., Liu, H. B., Wang, J., & Gu, Q., 2014, ApJ, 790, 84
Lu, X., Zhang, Q., Kauffmann, J., et al. 2017, ApJ, 839, 1
Lundquist, M. J., Kobulnicky, H. A., Kerton, C. R., et al. 2015, ApJ, 806, 40
Ma, B., Tan, J. C., & Barnes, P. J. 2013, ApJ, 779, 79
Mangum, J. G., & Wootten, A. 1993, ApJS, 89, 123
Mangum, J. G., Wootten, A., & Plambeck, R. L. 1993, ApJ, 409, 282
Mangum, J. G., Wootten, A., & Barsony, M. 1999, ApJ, 526, 845
Mangum, J. G., Darling, J., Menten, K. M., & Henkel, C. 2008, ApJ, 673, 832
Mangum, J. G., Darling, J., Henkel, C., et al. 2013a, ApJ, 779, 33
Mangum, J. G., Darling, J., Henkel, C., & Menten, K. M. 2013b, ApJ, 766, 108
Maud, L. T., Lumsden, S. L., Moore, T. J., et al. 2015, MNRAS, 452, 637
Mauersberger, R., Henkel, C., Wilson, T. L., et al. 1986, A&A, 162, 199
Mauersberger, R., Henkel, C., & Wilson, T. L. 1987, A&A, 173, 352
Mauersberger, R., Henkel, C., Weiß, A., et al. 2003, A&A, 403, 561
Melo, V. P., Pérez García, A. M., Acosta-Pulido, J. A., et al. 2002, ApJ, 574, 709
Merello, M., Evans, N. J. II, Shirley, Y. L., et al. 2015, ApJS, 218, 1
McCauley, P., Mangum, J. G., & Wootten, A. 2011, ApJ, 742, 58
Mitchell, G. F., Johnstone, D., Moriarty-Schieven, G., et al. 2001, ApJ, 556, 215
Molinari, S., Brand, J., Cesaroni, R., & Palla, F. 1996, A&A, 308, 573
Molinari, S., Pezzuto, S., Cesaroni, R., et al. 2008, A&A, 481, 345
Molinari, S., Merello, M., Elia, D., et al. 2016, ApJ, 826, 8
Mueller, K. E., Shirley, Y. L., Evans, N. J. II, et al. 2002, ApJS, 143, 469
Mühle, S., Seaquist, E. R., & Henkel, C. 2007, ApJ, 671, 1579
Myers, P. C., Ladd, E. F., & Fuller, G. A. 1991, ApJ, 372, L95
Nagy, Z., van der Tak, F. F. S., Fuller, G. A., et al. 2012, A&A, 542, A6
Ott, J., Weiß, A., Staveley-Smith, L., et al. 2014, ApJ, 785, 16
Pan, L., & Padoan, P. 2009, ApJ, 692, 594
Qin, S. L., Zhao, J. H., Moran, J. M., et al. 2008, ApJ, 677, 353
Reiter, M., Shirley, Y. L., Wu, J., et al. 2011, ApJS, 195, 1
Ridge, N. A., Wilson, T. L., Megeath, S. T., et al. 2003, AJ, 126, 286
Rosolowsky, E., Dunham, M. K., Ginsburg, A., et al. 2010, ApJS, 188, 123
Saito, H., Mizuno, N., Moriguchi, Y., et al. 2001, PASJ, 53, 1037
Sasselov, D. D., & Rucinski, S. M. 1990, ApJ, 351, 578
Schenck, D. E., Shirley, Y. L., Reiter, M., & Juneau, S. 2011, AJ, 142, 94
Schnee, S., Rosolowsky, E., Foster, et al. 2009, ApJ, 691, 1754
Schuller, F., Menten, K. M., Contreras, Y., et al. 2009, A&A, 504, 415
Shirley, Y. L. 2015, PASP, 127, 299
Stephens, I. W., Jackson, J. M., Whitaker, J. S., et al. 2016, ApJ, 824, 29
Tang, X. D., Esimbek, J., Zhou, J. J., et al. 2013, A&A, 551, A28
Tang, X. D., Henkel, C., Menten, K. M., et al. 2017a, A&A, 598, A30
Tang, X. D., Henkel, C., Chen, C.-H. R., et al. 2017b, A&A, 600, A16
Tang, X. D., Henkel, C., Menten, K. M., et al. 2018, A&A, 609, A16
Tomono, D., Terada, H., & Kobayashi, N. 2006, ApJ, 646, 774
Urquhart, J. S., Morgan, L. K., Figura, C. C., et al. 2011, MNRAS, 418, 1689
Urquhart, J. S., Moore, T. J. T., Csengeri, T., et al. 2014, MNRAS, 443, 1555
Urquhart, J. S., Figura, C. C., Moore, T. J. T., et al. 2015, MNRAS, 452, 4029
Urquhart, J. S., König, C., Giannetti, A., et al. 2018, MNRAS, 473, 1059
van der Tak, F. F. S., van Dishoeck, E. F., & Caselli, P. 2000a, A&A, 361, 327
van der Tak, F. F. S., van Dishoeck, E. F., Evans, N. J. II, & Blake, G. A. 2000b, ApJ, 537, 283
van der Tak, F. F. S., Black, J. H., Schöier, F. L., et al. 2007, A&A, 468, 627
Wang, K., Wu, Y. F., Ran, L., Yu, W. T., & Miller, M. 2009, A&A, 507, 369
Watanabe, T., & Mitchell, G. 2008, AJ, 136, 1947
Wienen, M., Wyrowski, F., Schuller, F., et al. 2012, A&A, 544, A146
Wienen, M., Wyrowski, F., Menten, K. M., et al. 2015, A&A, 579, A91
Wiesenfeld, L., & Faure, A. 2013, MNRAS, 432, 2573
Wouterloot, J. G. A., Walmsley, C. M., & Henkel, C. 1988, A&A, 203, 367
Wu, J., Evans, N. J. II, Gao, Y., et al. 2005, ApJ, 635, L173
Wu, Y., Zhang, Q., Yu, W., et al. 2006, A&A, 450, 607
Wu, J., Evans, N. J. II, Shirley, Y. L., et al. 2010, ApJS, 188, 313
Yu, N., & Xu, J. 2016, ApJ, 833, 248
Yuan, J. H., Wu, Y. F., Ellingsen, S. P., et al. 2017, ApJS, 231, 11
Zhang, Z. Y., Gao, Y., Henkel, C., et al. 2014, ApJ, 784, L31
Zylka, R., Güsten, R., Henkel, C., & Batrla, W. 1992, A&AS, 96, 525